DISSERTATION

RELATIVISTIC PLASMA NANO-PHOTONICS FOR ULTRA-HIGH ENERGY DENSITY PHYSICS

Submitted by

Michael Anthony Purvis

Department of Electrical & Computer Engineering

In partial fulfillment of the requirements

For the Degree of Doctor of Philosophy

Colorado State University

Fort Collins, Colorado

Fall 2014

Doctoral Committee:

Advisor: Jorge J. Rocca

Azer P. Yalin
Carmen S. Menoni
Mario C. Marconi

ABSTRACT

RELATIVISTIC PLASMA NANO-PHOTONICS

FOR ULTRA-HIGH ENERGY DENSITY PHYSICS

The trapping of femtosecond laser pulses of relativistic intensity deep within ordered nanowire arrays is shown to volumetrically heat near solid density matter transforming it into ultra-hot highly ionized plasmas. The plasmas were generated by focusing intense ~ 60 femtosecond duration ultra-high-contrast laser pulses onto targets consisting of arrays of densely packed vertically aligned nanowires 35-80 nm diameter. X-ray spectra are presented showing that irradiation of Ni and Au nanowire arrays heats a plasma volume several μm in depth to reach extraordinarily high degrees of ionization (i.e. 26 times ionized Ni , 52 times ionized Au), in the process generating gigabar level pressures. Electron densities nearly 100 times greater than the typical critical density and multi-keV temperatures are achieved using laser pulses of only 0.5 J energy. The large plasma volume and high electron density lead to an increased hydrodynamic-to-radiative lifetime ratio that results in a significant increase in X-ray yield. Measurements from a filtered photodiode array reveal a 100X increase in emission with respect to polished flat targets for photons with energies greater than 9keV. Scaling to higher laser intensities promises to create plasmas with temperatures and pressures approaching those in the center of the sun.

ACKNOWLEDGEMENTS

I would like to thank my advisor, Jorge Rocca for his support, guidance, encouragement and for the opportunities he provided throughout my education. I would also like to thank my committee members, Carmen Menoni, Mario Marconi and Azer Yalin for their support.

I've had the good fortune of working with many talented individuals on projects that have contributed to my education. I would like to specifically thank the following people: Jorge Filevich and Jonathan Grava for a wonderful collaboration during the plasma interferometry experiments; Nina Rohringer for several thrilling experimental campaigns at SLAC; Jim Dunn, Steve Moon and Marty Marinak, for providing an educational and rewarding experience with Lawrence Livermore National Labs.

I would like to acknowledge several people for their help with the nanowire experiments: Yong Wang, Shoujun Wang, Liang Yin and Brad Luther for their assistance with the Ti:Sapphire laser; Duncan Ryan and Mark Woolsten for contributions to the nanowire experimental setup; Reed Hollinger and Clayton Bargsten for their help carrying out the experiment and for the development of nanowire targets; Vyacheslav Shlyaptsev and Alexander Pukov for developing theory and models and for reviewing sections of my dissertation.

Most importantly I want to acknowledge the support of my wife, Stephanie and that of my family. I would like to thank them for their patience and encouragement throughout my entire education.

TABLE OF CONTENTS

LIST OF FIGURES

Chapter 1: Introduction

A new class of ultra-high-energy density experiments is underway, made possible by the development of high intensity short pulse lasers based on chirped pulse amplification [1]. With peak powers in the range of 10^{13}- 10^{15} W these lasers produce unsurpassed power densities in the laboratory. A single laser pulse can transform matter into very highly excited plasma containing multi keV electrons, ions, and photons with energies ranging from visible light to hard X-rays. This capability is making it possible to produce new physical phenomena in the laboratory such as solid materials with Gbar level pressures, fast ignition plasmas for experiments in nuclear fusion [2], to reproduce on a small-scale fascinating astrophysical phenomena [3], and the generation of large scale population inversions in plasmas resulting in soft X-ray laser amplification [4, 5].

There is a strong interest in using ultra-high-energy density plasmas to produce intense bursts of X-ray radiation for applications in backlighting dense objects [6, 7], ultrafast micrometer scale imaging [8], probing of structural changes in materials [9, 10]. These X-ray sources also have applications that include radiography of dense objects and phase contrast imaging of biological systems, a technique that reveals information beyond the limits of contrast radiography [8]. Additionally, there is an application in the technique of ultra-fast time-resolved X-ray diffraction that provides direct measurements of changes in atomic structure of physical systems [11, 10], as well as playing a significant role in fusion research as back-lighters for probing dense quickly evolving high density plasmas [6, 7].

As feature sizes of interest decrease, time scales approach shorter durations, or as plasmas become denser and more difficult to probe, the demands placed on a bright X-ray source become increasingly difficult to achieve. To meet these demands, sources must produce a greater number of photons in shorter pulse durations, at higher laser repetition rates and the photon energy must increase. A more complete review of high energy density plasmas is found in section 1.5 of this dissertation.

1.1 Intense Femtosecond laser irradiation of aligned nanowire arrays

This dissertation describes a new volumetric heating scheme that allows access to extreme plasma parameters that are highly efficient emitters of very bright bursts of X-rays. This is accomplished using a high-intensity high-contrast laser pulse to irradiate a structured target that consists of arrays of high-aspect ratio, vertically aligned nanowires, see publication in the Appendix [12]. An artistic drawing illustrates the interaction of the laser pulse with the nanowire array can be seen in Figure 1. The highly packed nanowire array targets have average densities that exceed the plasma critical density by orders of magnitude. In fact, the average density can be as high as 30% that of a solid target, where the average density is dictated by the spacing of the solid wires within the array. Unlike, the interaction with a solid target the nanowire array target allows the femtosecond laser to propagate deep into high density material, where the laser pulse is nearly totally absorbed.

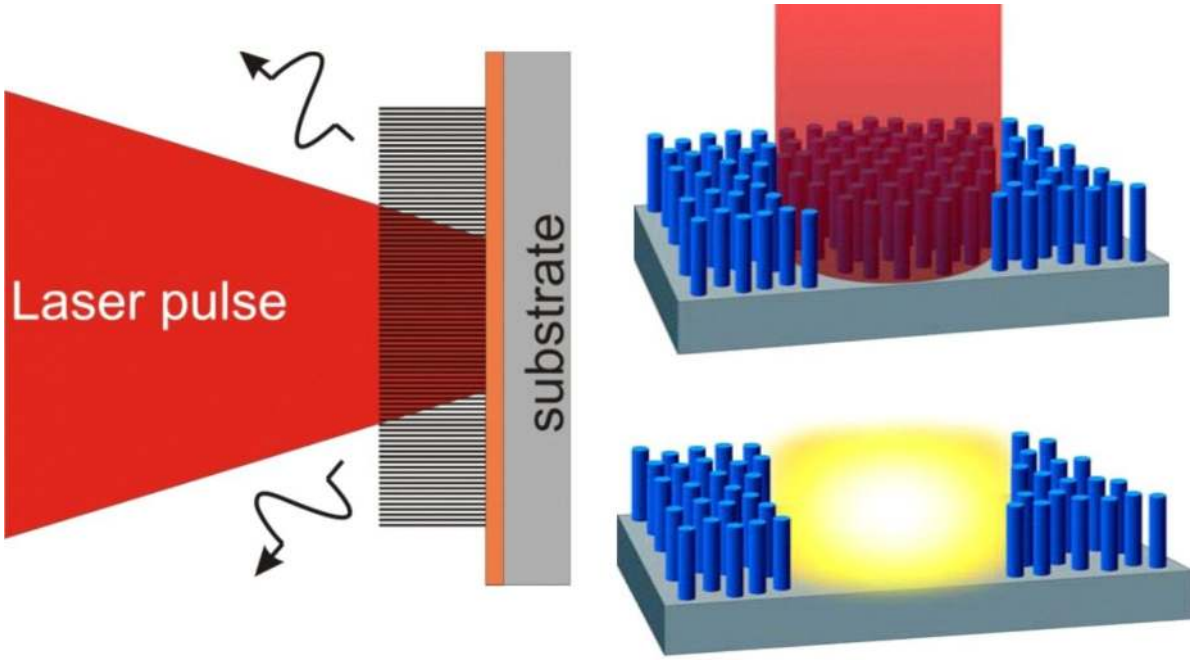

Figure 1. Illustration describing the interaction of the femtosecond laser pulse with a target consisting of an dense array of vertically aligned nanowires. A femtosecond laser pulse penetrates deep into the array volumetrically heating the plasma before the nanowires explode and expand closing the gaps. At this point a critical density forms impeding further penetration of the laser energy deep into the array.

The technique requires a very high contrast femtosecond laser pulse that is necessary to prevent the premature destruction of the nanowires and the formation of a plasma critical surface that can block the laser light from accessing the volume of the nanowire array, described in more detail in the following sections. The combination of high contrast and short pulse durations, and nanowire alignment, is what allows the femtosecond laser pulse to travel deeper into the array and to deposit laser energy throughout the nanowire volume. This allows the laser to heat large volumes of high density target material, where the conditions for most efficient X-ray generation can be realized.

Atomic rates calculations allow for comparison of radiation loss rates per electron and per ion of different radiation processes as a function of plasma temperature for different electron densities. Calculations performed by V. Shlyaptsev using the code ATOM are shown in Figure 2 [13]. Photo recombination is seen to dominate radiative losses for higher density plasmas of electron densities ~10^{24}cm^{-3} (see Figure 2B) while line radiation governs radiative losses for the lower density 10^{21} cm^{-3}plasma (see Figure 2A). Computation of the total radiated energy per unit volume is proportional Ni^2 and is expected to be much higher.

The radiative cooling time is defined as the time required to radiate the entire thermal energy contained within the volume. The thermal energy volume is expressed as,

$$Thermal\ energy\ in\ volume\ V = \frac{3}{2} K\ Te\ Ne\ V \quad [Jcm^{-3}]$$

where Te is the electron temperature, Ne is the electron density and V is the radiating volume. The radiative cooling time is computed using the radiation loss rates in Figure (A) and (B) in the following way,

$$Radiation\ cooling\ time\ [s] = \frac{Thermal\ energy\ \ in\ volume\ V}{Rad.loss.rate\ x\ Ne\ x\ Nion\ x\ V}$$

The computed radiation cooling time is compared to the hydrodynamic time in Figure 2C and 2D as a function of temperature. The shortest time scale determines the dominant cooling mechanism. Here the hydrodynamic time has been defined as $\tau = {\Delta L}/{C_s}$ where the plasma dimension is taken as ΔL=10μm to allow simplicity of comparison and Cs is the plasma sound speed given by $C_S = \sqrt{{ZkTe}/{Mi}}$. In the lower density plasma (Figure 2C), line radiation is much slower than the typical hydrodynamic time scales, whereas in the higher density plasma (figure

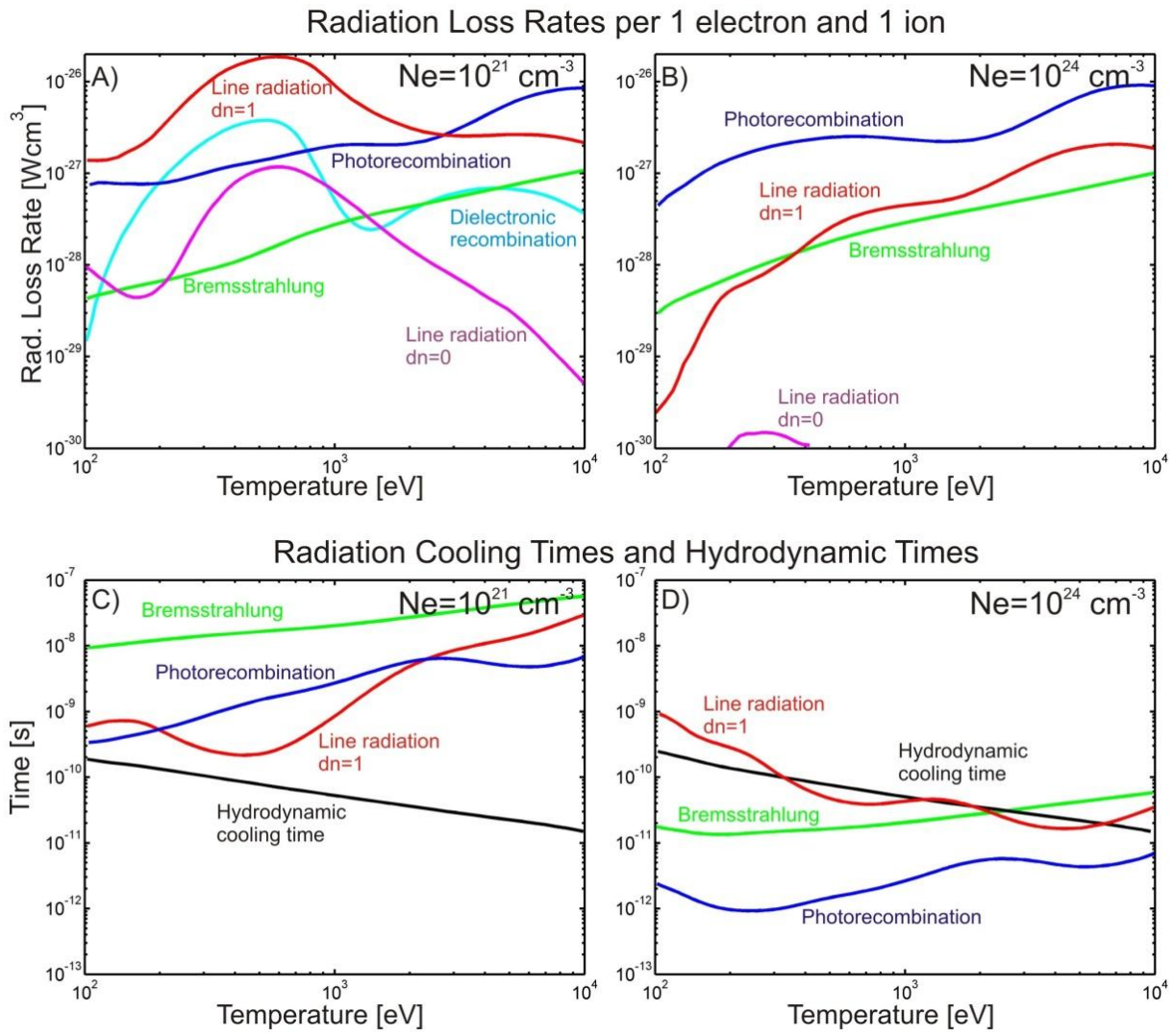

Figure 2. The radiative loss rates per electron and per ion for two different densities A) Ne=10^{21} cm^{-3} and B) Ne=10^{24} cm^{-3} as functions of the electron temperature and the respective radiative and hydrodynamic cooling times (C) and (D). Atomic rates were computed assuming the plasma is optically thin and are calculated per electron per ion. Photorecombination dominates radiative losses for the higher density plasmas. The radiative cooling time is also compared to the hydrodynamic time for both densities. In these plots, the shortest time scale determines the strongest mechanism. For the higher density plasma D) 10^{24} cm^{-3}, photorecombination is much faster than the typical hydrodynamic time scale, where the lower density plasma C) 10^{21}cm^{-3} is governed by the hydrodynamic time scales. Computations were performed by V. Shlyaptsev using the code ATOM.

2D) photorecombination greatly exceeds the typical hydrodynamic time scale by more than 2 orders of magnitude. The ratio of radiative cooling to hydrodynamic time determines whether the plasma is cooled primarily through radiation or through expansion. The conditions for most efficient X-ray generation occur when the radiation loss rate greatly exceeds the hydrodynamic lifetime, this ratio is >1 in the higher density plasma for temperatures from 100-10keV, see Figure 2D.

1.2 The absorption of light into a flat solid target

Before a plasma is formed, light interacting with the solid surface is only capable of penetrating up to the skin depth of the solid, < 2nm deep for a laser wavelength of λ=400nm incident on polished Cu. Absorption up to this skin depth occurs through the mechanism of joule heating where the surface temperature increases until it reaches the evaporation temperature. Further absorption of laser light, accompanied by an increase in laser intensity, will cause ionization of the evaporated target material to occur and the formation of a plasma. Once plasma has been formed, the mechanisms of laser light absorption fundamentally change.

The absorption of light strongly depends on laser parameters like intensity and wavelength. When the field of the laser is strong enough it will force electrons to oscillate with a velocity Vosc, given by,

$$\frac{Vosc}{c} = \frac{e \cdot E}{m_e \cdot \omega} = \sqrt{\frac{I \cdot \lambda^2}{1.39 * 10^{10}\, {}^{W}/_{cm^2\, \mu m^2}}}$$

where intensity, I is in units of 10^{10} Wcm^{-2} and wavelength λ is in units of μm. This is the well known $I\lambda^2$ relationship used to describe threshold intensity for characteristic regimes of laser absorption. For instance, inverse bremsstrahlung or collisional absorption starts to become less

efficient around $I\lambda^2 \geq 10^{15}$, [14]. At this point resonant absorption becomes important, a process where the electric field of the laser pulse perpendicular to the target surface tunnels through the critical surface, where it resonantly pumps a plasma wave heating the electrons within the plasma [15]. Likewise, the mechanism known as vacuum heating, first pointed out by Brunel [16], is generally more efficient when $I\lambda^2 \geq 10^{18}$. This is a process where the laser electric field rips electrons away from the target surface during half a cycle, accelerating them in the direction of the vacuum along the large density gradients in the plasma. A space charge turns the electrons around where they now see the reversed field and consequently are accelerated back into dense plasma near the target surface. The electrons have now gained kinetic energy that can be transferred into the plasma through collisions.

Laser energy deposition into a solid density plasma is fundamentally limited by the depth at which laser light can penetrate. The dispersion relationship for an EM wave in a plasma is given by,

$$\omega^2 = {\omega_{pe}}^2 + kc^2$$

where ω is the angular frequency of the laser light, ω_{pe} is the plasma frequency and k is the wave vector. If the laser frequency is less smaller than the plasma frequency, $\omega < \omega_{pe}$, the wave vector k becomes imaginary and the electrons shield the wave. As a result, the condition where $\omega_{pe}=\omega$ defines the maximum density to which light can penetrate the plasma. The corresponding electron density is known as the critical density and is given by,

$$n_{crit} = \frac{\pi c^2 m_e}{\lambda^2 e^2} \cong \frac{1.1 \times 10^{21}}{\lambda[\mu m]^2}$$

where, m_e is the mass of the electron, e is the charge and c is the speed of light. For a typical λ=1μm laser, this density is a few orders of magnitude below that of solid density. A commonly used 1D illustration of the density and temperature contours for a typical laser-heated planar target is shown in Figure 3. Upon interaction with the solid target light from the laser pulse is absorbed in a region with density just below the critical density surface. Only a small fraction, (in some cases <10%) of a femtosecond laser energy is used to heat the plasma. The rest of the light is reflected away by the same mirror-like critical density plasma surface. This limitation prevents directly heating a large volume near-solid density material with an optical laser pulse. As described in the previous section, the lower density plasma conditions results in a decreased radiative to hydrodynamic time ratio. This combination of reduced radiative to hydrodynamic time ratio, low absorption, and low density is responsible for the typically low conversion efficiency (CE < 0.0001) of laser pulse energy to X-ray emission (hv>1keV) observed in solid slab targets [17, 18, 19]. The challenge is to find ways to improve the laser/target interaction to maximize the coupling of the laser's energy into the target surface, thereby generating denser hot plasmas that most efficiently produce X-rays.

1.3 Overcoming the critical density barrier with nanowire array targets

High contrast femtosecond laser pulse irradiation of nanowire array targets can overcome the critical surface limitation because the laser light is allowed to propagate deep inside the nanowire array where it can heat a volume of near solid density material (right on Fig. 4). Laser light in this illustration can be seen to penetrate deep into the array where it is nearly fully absorbed into high density material. This is in contrast to the heating of thin low density surface layer in a solid target plasma (left side of Fig. 4).

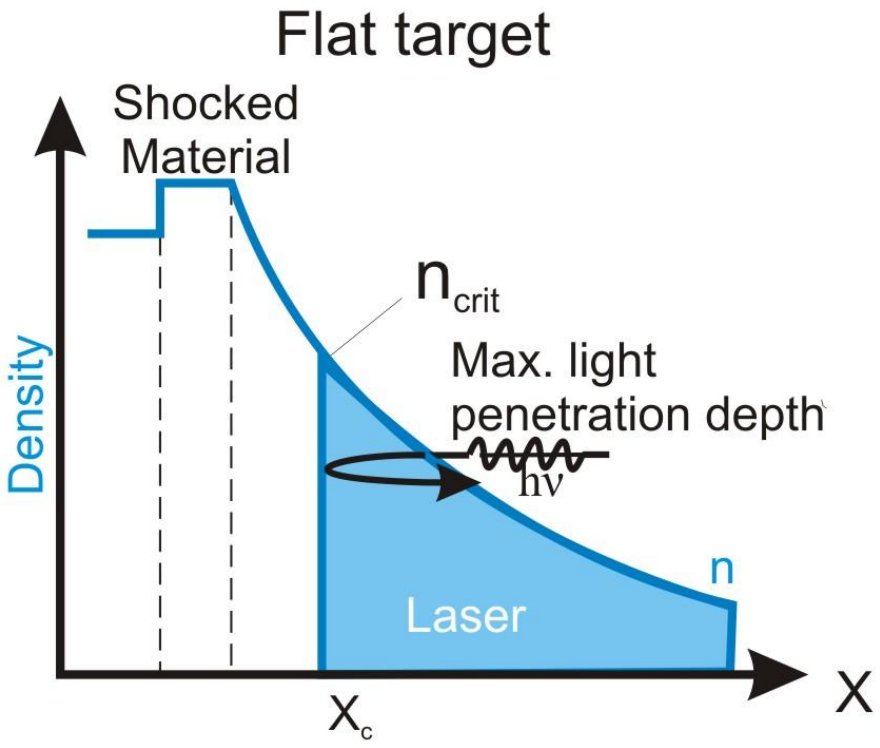

Figure 3. 1D profile of the electron density in the direction normal to a solid target surface. Light is absorption is limited to the plasma critical density, n_{crit}, where it is reflected back through the plasma. Although in most plasmas the laser light is absorbed in lower density regions and only a fraction reaches this surface. This limitation prevents directly depositing laser pulse energy into supra-critical density material.

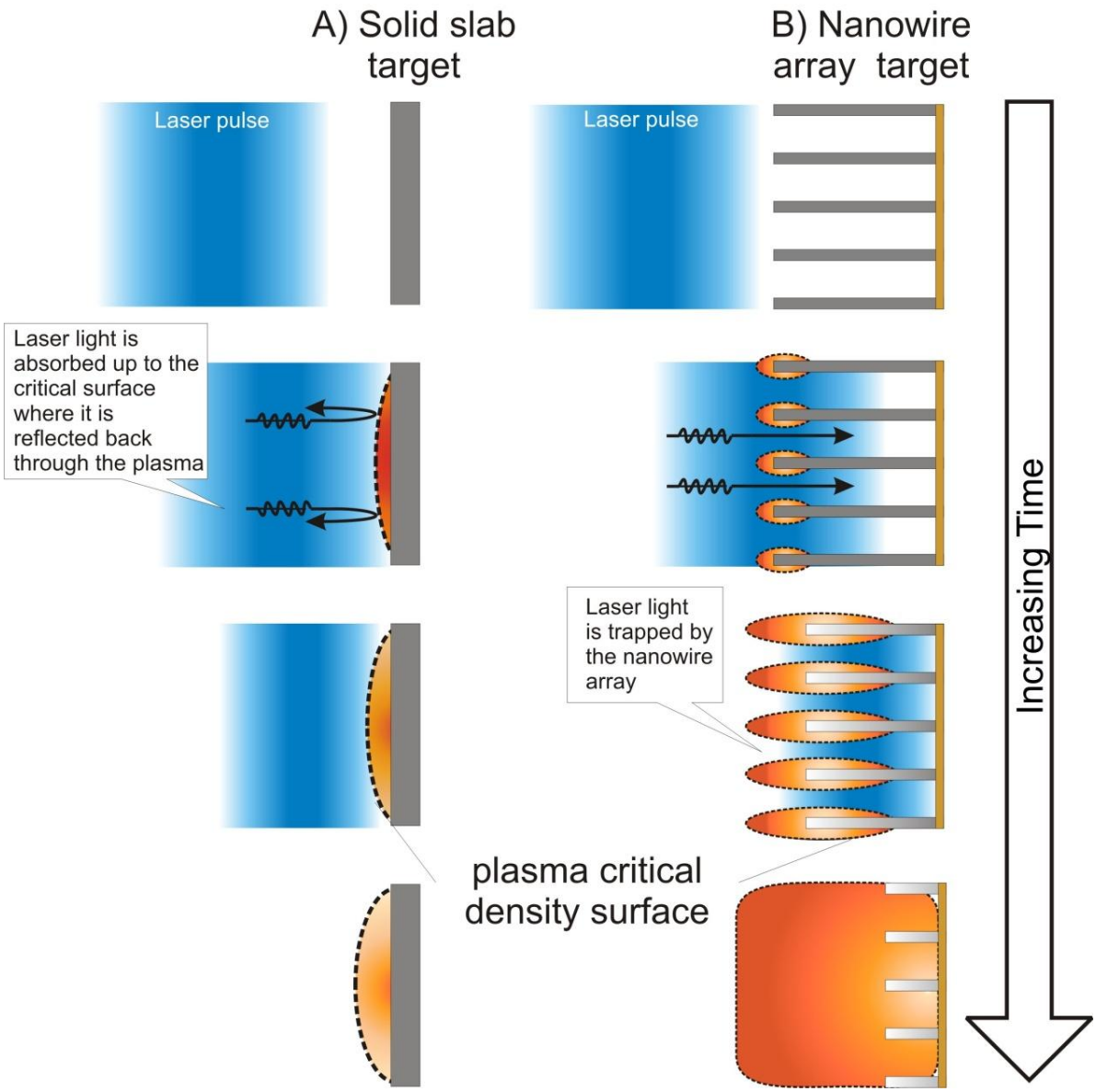

Figure 4. Comparisons of plasmas resulting from irradiation of: (A) solid slab target, (B) array of aligned nanowires. The advantage of femtosecond laser propagation into a nanowire array (right) is that light is allowed to propagate deep into higher density material where it is nearly totally absorbed, whereas light incident on the flat target (left) is reflected from the plasma critical surface at a lower density and is not completely absorbed. The heated nanowires laterally expand to fill the space between the wires.

The high intensity femtosecond laser pulse interacting with the nanowire array pulls electrons from the nanowire surface by optical field ionization and accelerates them into the gaps between the nanowires during half a cycle. A space charge effect then turns the electrons around and when the field reverses the electrons are accelerated back into the nanowire, where they collide [16]. Electron-impact ionization increases the electron density and a hot plasma is formed as the laser energy is transferred into thermal energy. Laser energy is first deposited near the tip of the nanowire array that then propagates along the nanowire. The heated and ionized nanowires expand into nearby nanowires closing off the vacuum gaps. The high speed at which the nanowire array gaps close off, places the requirement of a fast and "clean" (free from pre-pulses) laser pulse. A femtosecond high contrast pulse is capable of depositing all of the energy before the gaps are closed, and it is possible to nearly fully absorb the light from the laser pulse. This effect provides a means to increase the plasma temperature over a large volume at near solid densities. In conclusion, the exploding nanowires fills the gaps with plasma, producing a heated volume, with a much larger density, than in the case of the flat target, see Fig. 4. The increased absorption, greatly increased plasma density, and increased radiative-to-hydrodynamic cooling time ratio, play strong roles in increasing the conversion efficiency of optical laser light into soft and hard X-rays.

1.4 Generation of ultra-high energy density plasmas

The generation of very high energy density plasmas is made possible with this technique that is capable of depositing a high energy density over a large volume. In fact, as discussed below, extraordinarily high degrees of ionization (52X ionized Au) can be obtained using laser pulses of only 0.5J of energy. Similar observations had only been previously achieved using laser pulses

with kiloJoule level energy [20], demonstrating that the scheme presented herein is extremely efficient in generating such extreme plasma conditions. An increase of 50-100X was measured for X-ray emission in the > 0.9 keV, > 9.6 keV spectral regions respect to solid flat nickel targets under the same irradiation conditions. Figure 5 shows compares the parameters of the nanowire array plasmas relative to other plasmas. The pressure in these ultra-high-energy-density plasmas are only exceeded by those created in the central hot-spot of the imploded fusion capsule in early National Ignition Facility (NIF) experiments at ultra-high laser energy [21].

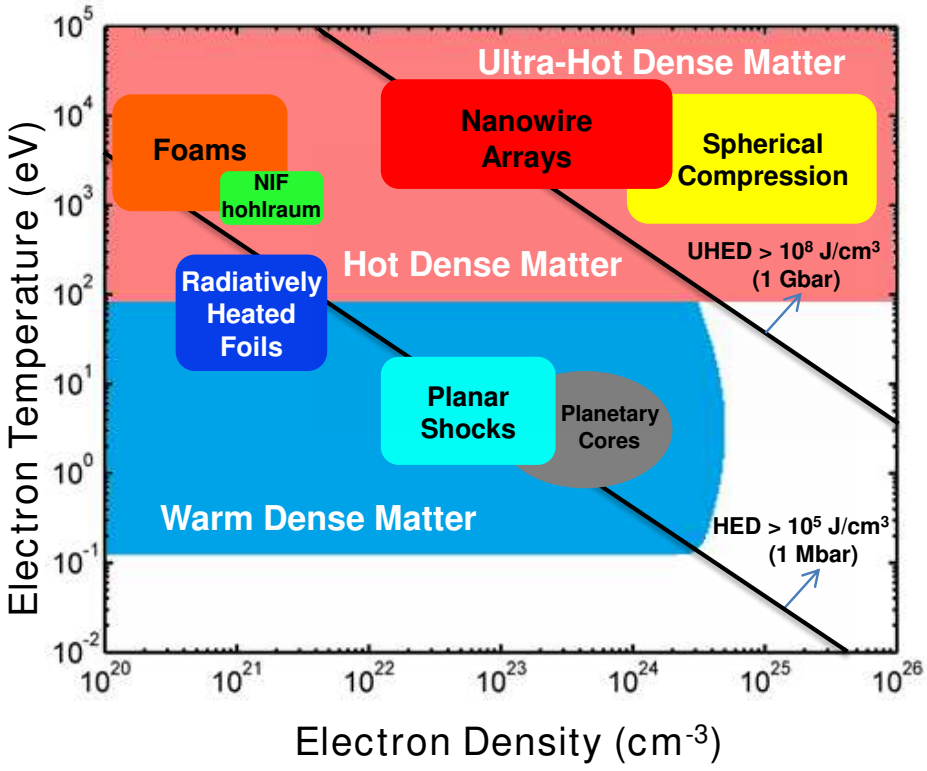

Figure 5. Parameter space of temperature-electron density showing the plasma regime accessible by irradiation of aligned nanowire arrays relative to other high energy density plasmas.

1.5 Previous studies of high energy density plasmas

Long-lived plasmas that are simultaneously dense and hot (multi-keV) have been created by spherical compression in fusion experiments at the world's largest laser facilities, and by supersonic heating of volumes with densities on the order of N_{ec} using multi-kJ lasers pulses [21, 22, 23, 24]**.** Such high energy laser pulses have ionized mid-atomic number (Z) plasmas to the He-like and H-like stages [25, 26], and have stripped high-Z elements such as Au to charge states neighboring the Ni-like ion[26, 27, 28]. Supersonic thermal conduction on a time scale faster than the hydrodynamic expansion and strong shock waves driven by high intensity ultra-short laser pulses can also create very hot near-solid density plasmas [29]**.** However, due to the relatively slow speed of the shock wave, the region with both high temperature and high density is narrow, typically ~ 0.1 μm [29, 30]**.** Petawatt laser irradiation of Cu foils with 0.7 ps duration laser pulses generated thin surface plasma layers with electron temperatures of 2-3 keV in which the Cu He-α line intensity exceeded that of the Cu K-α line [31]. Recently, high contrast laser pulses from a Petawatt laser were reported to heat a plastic target to an electron temperature of 600 eV at a 30 μm depth [33] Experiments with lower density targets have also produced volumetrically heated plasmas with high temperatures. Heating of 10% solid density Cu foams with a 0.93 kJ pulse produced 1.5 times greater He-like line emission than a Cu foil [35]. Irradiation of clusters has been shown to create plasmas with multi-keV thermal electrons and extremely energetic ions, but with only moderate average densities [37].

In turn, experiments that monitored the X-ray emission from plasmas created irradiating structured targets [39, 35, 36, 37], "smoked" targets[38, 39], and nanowire arrays [39, 40, 41, 42] have shown large increases in X-ray flux, which suggest the formation of a hot-dense plasma and/or enhanced hot electron production. Conversion efficiencies (C.E.) of 10^{-4} -10^{-2}

have been reported for X-rays >1keV, demonstrated utilizing target surfaces including, nanolithographic gratings and soot clusters [17, 35, 39]. In particular, the irradiation of arrays of 0.8-1 μm long Ni nanowires with picosecond laser pulses has produced up to 50 times greater emission than a flat target in the ~ 1 keV photon region and total X-ray yields of 0.2 percent [39]. The irradiation of Au nanowire arrays showed a 20 fold increase in soft X-ray emission [42]. Even with relatively low laser intensities I= 10^{16} Wcm^{-2}, hard X-rays in the 10-100keV range have been produced by fs irradiation of nano-size dielectric spheres or ellipsoids with CE of ~10^{-9} [36, 37]. Similarly, when nanowire targets were employed, X-ray yields (100-300keV) surpassed yields from polished flat targets by more than ~40X [40]. Hard X-ray emission (>100keV) from clustered nanorods was found to jointly depend on the aspect ratio of the nanorods and the cluster size, suggesting that the technique of irradiating nanowire arrays to produce X-rays may be further optimized for greater yields.

The next section discusses details of the experimental setup including the synthesis of vertically aligned nanowires, the generation of a high intensity, high contrast laser pulse and the X-ray diagnostics used. Chapter 3 follows with results using the volumetric heating approach to create plasmas with KeV temperatures and densities approaching 100 times the plasma critical density. Results on X-ray yield from the ultra-high energy density plasmas are also presented. The results have been published in the journal Nature Photonics, shown in Appendix 1.

References

1. Strickland D. & Mourou G. Compression of amplified chirped optical pulses. *Opts. Communications*. **40** 437 (1982).
2. Tabak M. et al., Ignition and high gain with ultrapowerful lasers, *Phys. of Plasmas* **1**, 1626, (1994).
3. Remington B. A., et al., Modeling astrophysical phenomena in the laboratory with intense lasers, *Science* **284**, 1488 (1999).
4. Keenan R. et al., High-Repetition-Rate grazing incidence pumped X-ray laser operating at 18.9 nm, *Phys. Rev. Lett*. **94** (2005).
5. Luther B.M. et al, Saturated high-repetition-rate 18.9nm tabletop laser in nickellike molybdenum, *Opt. Lett.* **30**, 165 (2005).
6. Marshall F. J. et al., Plasma-Density Determination from X-ray Radiography of Laser-Drive Spherical Implosions, *Phys. Rev. Lett.,* **102**, 185004 (2009).
7. Callahan D.A., et al. The velocity campaign for ingnition on NIF, *Phys. Plasmas* **19** (2012).
8. Laperle C.M. et al., Propagation based differential phase contrast imaging and tomography of murine tissue with a laser plasma X-ray source, *App. Phys. Lett*. **9**1 (2007).
9. Neutze R. et al., Potential for biomolecular imaging with femtosecond X-ray pulses, *Nature* **406**, 17 (2000).
10. Rousse A. et al., Non-thermal melting in semi-conductors measured at femtosecond resolution, *Nature* **410**, 65 (2001).
11. Ben-Nun M., Cao J., & Wilson K.R. Ultrafast X-ray and electron diffraction: Theoretical Considerations, *Phys. Chem. A*. **101**, 47 (1997).
12. Purvis M.A. et al. Relativistic plasma nano-photonics for ultra-high energy density physics, *Nature Photonics* **7**, 796-780 (2013).
13. Sobelman L., Vainshtein LA, Yukov EA, Excitation of Atoms and Broadening of Spectral Lines. *Springer,* Berlin, (1981).
14. Cui Yun-Qian, et al. Laser absorption and hot electron temperature scaling in laser-plasma interactions, *Plasma Phys. Control Fusion*, **55** (2013).
15. Freidberg J.P., Mitchell R.W., Morse R.L., Rudsinski L.I., Resonant Absorption of Laser Light by Plasma Targets. *Phys. Rev. Lett*., **28**, 795-799 (1972).
16. Brunel F. Not-so-resonant, resonant absorption. *Phys. Rev. Lett*., **59**, 52-55 (1987).

17. Murnane M.M. et al. Efficient coupling of high-intensity subpicosecond laser pulses into solids. *Appl. Phys. Lett*., **62**, 1068-1070 (1993).
18. Milchberg H. M. & Freeman R. R. Light absorption in ultrashort scale length plasmas. J. *Opts. Soc. Am. B,* **6**, 1351-1355 (1989).
19. Price, D.F., et al. Absorption of ultra-short laser pulses by solid targets heated rapidly to temperatures 1-1000eV, *Phys. Rev. Lett*., **75** (1995).
20. Hoarty D.J., et al, Observations of the effect of ionization-potential depression in hot dense plasma, *Phys. Rev. Lett.*, **110** (2013).
21. Glenzer S. H. et al. Cryogenic thermonuclear fuel implosions on the National Ignition Facility. *Phys. Plasmas*. **19**, 1228-1231 (2012).
22. Glenzer S. H. et al. Symmetric inertial confinement fusion implosions at ultra-high laser energies. *Science*. **327**, 1228-1231 (2010).
23. Fujiota S. et at. X-ray astronomy in the laboratory with a miniature compact object by laser-driven implosion. *Nature Physics*, **5**, 821-825, (2009)
24. Robey H. F. et al. Hohlraum-Driven Mid-Z (SiO2) Double-shell implosions on the Omega laser facility and their scaling to NIF. *Phys. Rev. Lett.* **103**, 145003 (2009).
25. Fournier K. B. et al. Efficient Multi-keV X-ray Sources from Ti-Doped Aerogel Targets. *Phys. Rev. Lett.*, **92**, 165005 (2004).
26. Matthews, D. L. et al. Characterization of laser produced plasma x ray sources for use in xray radiography. *J. Appl. Phys.,* **54**, 4260-4268 (1983).
27. Foord M. E. et al., Ionization processes and charge-state distribution in a highly ionized high-Z Laser-produced plasma. *Phys. Rev. Lett.* **85**,992-995 (2000).
28. Heeter R. F. et al., Benchmark measurements of the ionization balance of non-local-thermodynamic-equilibrium gold plasmas. *Phys. Rev. Lett.,* **99**, 195001 (2007).
29. Young B.K.F., Wilson B.G., Price D.F., Stewart R.E. Measurement of X-ray emission and thermal transport in near-solid-density plasmas heated by 130 fs laser pulses. *Phys. Rev. E*, **58** 4929-4936 (1998).
30. Guethlein G., Foord M.E., Price D. Electron temperature measurements of solid density plasmas produced by intense ultrashort laser pulses. *Phys. Rev. Lett.,* **77**, 1055-1058 (1996).
31. Theobald W. et al. Hot surface ionic line emission and cold K-inner shell emission from petawatt-laser-irradiated Cu foil targets. *Phys. Plasmas* **13**, 043102 (2006).

32. Hobbs L.M. et al. Demonstration of short pulse laser heating of solid targets to temperatures of 600 eV at depths of 30um using the Orion high power laser. *Bulletin of the American Physical Society*, **57**, 156 (2012).
33. Huntington C.M. et al. Spectral analysis of X-ray emission created by intense laser irradiation of copper materials. *Rev. Sci. Instrum.*, **83**, 10E114 (2012).
34. Ditmire T., et al., High-energy ions produced in explosions of superheated atomic clusters. *Nature*, **386**, 54-56 (1997).
35. Gordon S.P., Donnelly T., Sullivan A., Mamster H., Falcone R.W. X-rays from microstructured targets heated by femtosecond lasers. *Opt. Lett.*, **19,** 484-487 (1994).
36. Rajeev P.P, Taneja P., Ayyub P., Sandhu A.S., Kumar G. Metal Nanoplasmas as Bright Sources of Hard X-ray Pulses. *Phys. Rev. Lett*, **90**, 115002 (2003).
37. Sumeruk, H.A. et al. Control of Strong-Laser-Field Coupling to Electrons in Solid Targets with Wavelength-Scale Spheres. *Phys. Rev. Lett.,* **98**, 045001 (2007).
38. Khattak, F.Y. et al. Enhanced He-α emission from "smoked" Ti targets irradiated with 400nm, 45 fs laser pulses. *Europhys. Lett.*, **72**, 242–248 (2005).
39. Kulcsár G. et al. Intense Picosecond X-ray Pulses from Laser Plasmas by Use of Nanostructured "Velvet" Targets. *Phys. Rev. Lett.*, **84**, 5149-5152 (2000).
40. Mondal S. et al. Highly enhanced hard X-ray emission from oriented metal nanorod arrays excited by intense femtosecond laser pulses. *Phys. Rev. B*, **83**, 035408 (2011).
41. Ovchinnikov A.V. et al. Characteristic X-rays generation under the action of femtosecond laser pulses on nano-structured targets. *Laser and Particle Beams*, **29**, 249–254 (2011).
42. Nishikawa T., Suzuki S., Watanabe Y., Zhou O., Nakano H. Efficient water-window X-ray pulse generation from femtosecond-laser-produced plasma by using a carbon nanotube target. *Appl. Phys. B*, **78**, 885-890 (2004).

Chapter 2: The experimental setup for generation and detection of X-rays from ultra-high energy density nanowire array plasmas.

This chapter focuses on the details of the experimental setup used in the nanowire array plasma experiments, covering the development of nanowire array targets, the generation of an intense high contrast femtosecond laser pulse and the suite of X-ray and soft x-ray diagnostics used for understanding the interaction of the high contrast femtosecond laser pulse with the nanowire array target.

2.1 Developing vertically aligned nanowire array targets

The synthesis of vertically aligned nanowires with high aspect ratio has been previously reported [1] and vertically aligned nanowires are even commercially available from Synkera Inc. [2]. The synthesis our own nanowire arrays was motivated by the desire to optimize X-ray emission through dependencies on properties of the nanowire targets such as length, density, uniformity, quality and straightness of the wires.

Nickel and Gold nanowires were synthesized by electro-deposition into porous alumina membranes. The process utilizes templates of anodized alumina oxide (AAO) whose pores run perpendicularly to the template; see the cross-section in Figure 6A. These commercially available pores are uniform in diameter and highly packed together, with pore densities as high as 30%, and pore diameters 30-250nm, although most of the development described herein focused on 35nm, 50nm and 80nm diameter wires with pore density of 12%.

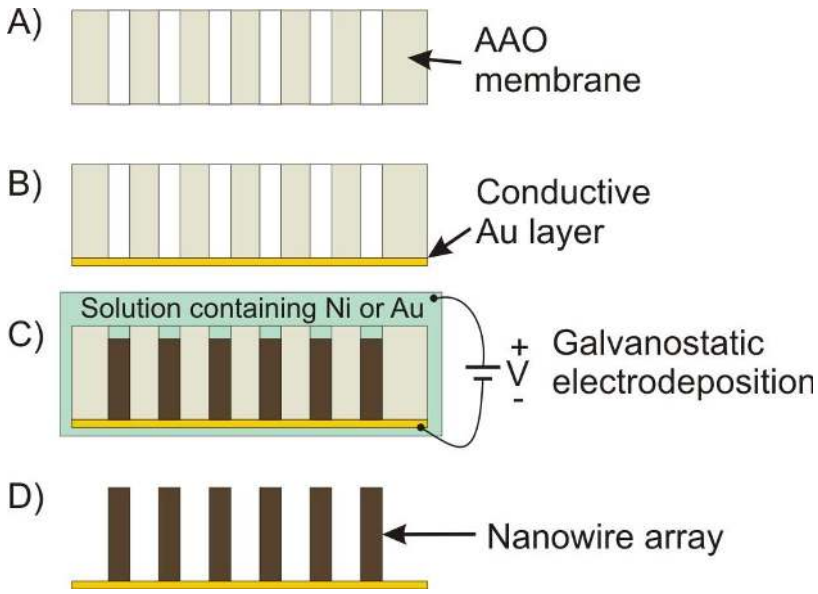

Figure 6. A graphical illustration of the synthesis of Ni or Au nanowire arrays.

Many different techniques have been explored to electrochemically develop nanowires using AAO templates [1, 3]. Our technique employs a thin conductive gold layer that is coated onto one side of the template to serve as an electrode and support structure for the free standing nanowires, Figure 6B. The template is placed in a Nickel or Gold solution where an electrostatic potential is applied causing metals in the solution to be deposited first at the bottom of the pore, where it begins to slowly fill the template (Figure 6C). The electrostatic potential is removed once the wires have reached a desired length.

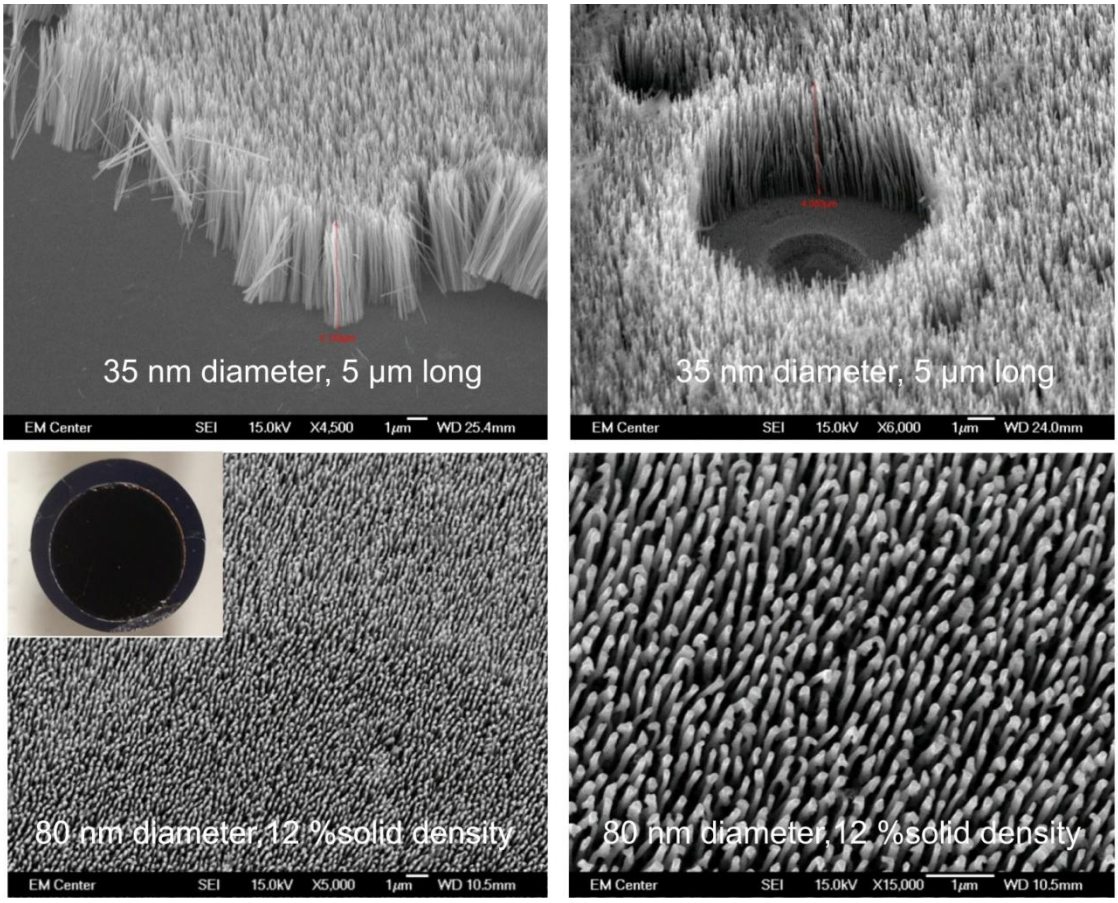

Figure 7. SEM images of arrays of vertically aligned Ni nanowire arrays.

Finally, the nanowire array is exposed when the AAO template is thoroughly dissolved in a 1M NaOH solution (Figure 6D). By applying this process, free-standing nanowire arrays can be formed across large surfaces. Cross-sectional images showing examples of the final result were taken using a Scanning Electron Microscope (SEM (Figure 7). The SEM images were also used to measure the diameter and length of the nanowires. SEM images were also acquired to assess wire uniformity at many different locations across a target, whose surface area was typically $>1cm^2$.

Wires with diameters of 35nm, 55 nm and 80nm were developed with aspect ratios in some cases >400, fabricated with densities between 7 % to 30% solid density. Figure 7 shows

examples SEM images that show the highly ordered vertically aligned Ni and Au nanowire array targets constructed using this fabrication process. The SEM image were taken with 4500X-15,000X magnification. The inset in Fig. 7 shows the Ni nanowire targets appear black in visible light, indicating a very high level of optical absorption. The diameter of this target is 10mm and the nanowires are uniform across the surface.

2.2 Experimental setup for the generation of a high-intensity high-contrast laser pulse

Arrays of vertically aligned Ni and Au nanowires were irradiated with ultra-high contrast (> $1x10^{11}$) pulses of ~ 60 fs FWHM duration from a frequency doubled (λ= 400 nm) high power Ti:sapphire laser. The ultra-high contrast is critical, as a relatively low intensity pre-pulse can destroy the array by forming a critical density surface prior to the arrival of the high intensity ultra-short pulse.

The Ti:Sapphire laser consisted of a Kerr mode locked [4] oscillator with 3 stages of amplification, capable of delivering pulses of up to 10 J energy before compression. A vacuum compressor with gold-coated gratings, designed with a clear aperture of 65mm diameter, temporally compressed pulses to ~ 60fs FWHM duration. To prevent damaging the gratings, the experiments discussed in this thesis utilized pulses up to 2J of energy in the fundamental 800nm wavelength. The compressed pulse duration was monitored at on a shot-to-shot basis using the powerful techniques of single-shot frequency resolved optical gating (FROG) [5, 6] performed at the fundamental wavelength. These techniques allow for measurement of the pulse intensity as a function of time and frequency, without having to make assumptions about the pulse shape. More recently, after the data for acquisition of the data for thesis was completed the frequency

doubled pulses were measured to have very similar pulse durations 60-70ns, using a FROG based on transient-grating geometry [7].

Contrast of the 1ω beam was measured using a third order scanning autocorrelator and was found to be limited to below ~$2x10^{-7}$ by an amplified spontaneous emission (ASE) pedestal preceding the main pulse, as illustrated in Figure 8.

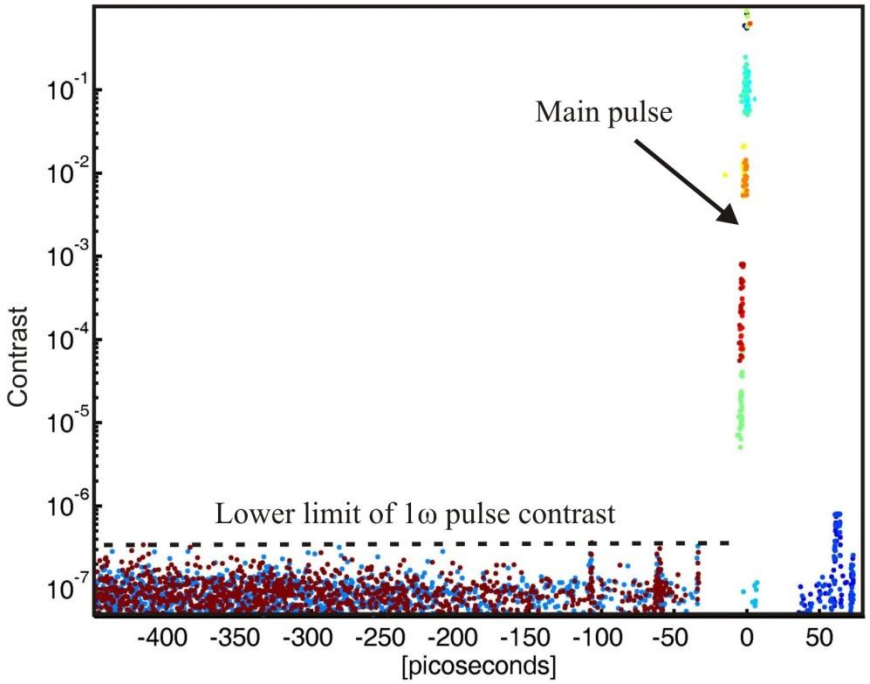

Figure 8. Result from a third order scanning auto-correlator showing that the pulse contrast of the 1ω beam is ~ $2x10^{-7}$.

The contrast is greatly improved by frequency doubling in a large aperture, 6 cm diameter, 0.8 mm thick, KDP Type I crystal with an efficiency of 40%. Four dichroic mirrors with coatings designed to reflect 99.9% of the 2ω and transmit 98.5% of the 1ω beam, were used to separate the 2ω beam from the fundamental, illustration shown in Figure 9. This set of mirrors is capable of reducing the 1ω component to 5 x 10^{-8}, therefore resulting in a contrast better than 1 x 10^{11}.

The pulse energy delivered to the target was measured on every shot by a pyroelectric energy meter placed after a 500 µm thick beam splitter with a coating designed to reflect 1% of the pulse energy. The 2ω beam was focused onto the target using an f =17.8 cm Al-coated off-axis parabolic mirror resulting in spot sizes < 10 µm in diameter. The targets were mounted on a precision motorized XYZ translation stage allowing for target displacement between shots to access to different regions of the target surface that had not been shot, while keeping the target surface in the focus of the laser.

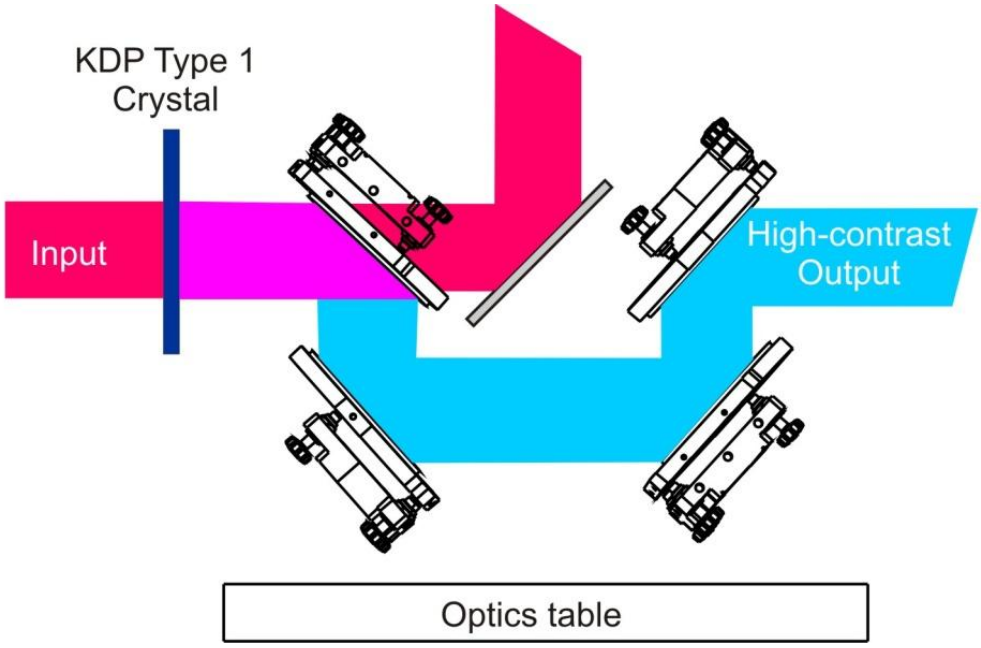

Figure 9. Illustration of the system of optics used to improve pulse contrast by second harmonic generation.

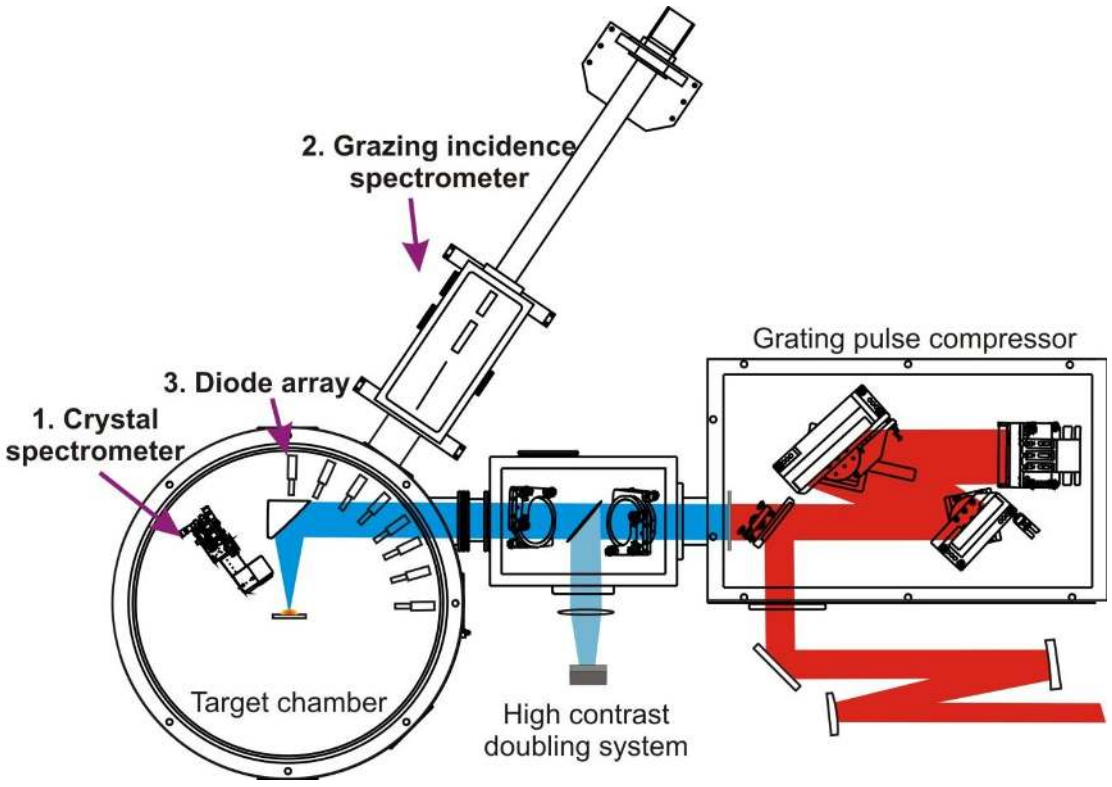

Figure 10. A schematic of the experimental setup used to generate ultra-hot dense plasmas by irradiation of arrays of vertically aligned nanowires.

2.3 Plasma diagnostic equipment

The detection of X-rays and soft X-rays radiated by the plasma was monitored using a suite of diagnostics. Figure 10, is a schematic of the experimental setup illustrating the set of diagnostics that includes a compact crystal X-ray spectrometer (1), a soft X-ray grating spectrometer (2) and an array of filtered semiconductor photodiodes (3). The principles, design and methods for detector calibration are described in further detail in the following sections.

2.3.1 The X-ray crystal spectrometer

An X-ray spectrometer can offer a great deal of information about a plasma, for instance spectral lines can be used to infer the degree of ionization and the plasma temperature and ionization state. It is a commonly used diagnostic, has been in use since around the 1930's [8], that is capable of generating spectra with very high spectral resolution. Crystal spectrometers are responsible for identifying a great number of the X-ray spectral lines known today, playing an important role in our understanding of atomic physics. They can also be used to identify the composition of materials based on their characteristic X-ray emission.

X-rays with wavelength <5Å, penetrate deeply into materials making it impossible to use traditional spectrometers based on diffraction gratings. For example, the reflection of Au at 2° grazing incidence is <10% at λ=6Å. An X-ray spectrum beyond this region can only be measured using diffraction from a crystal. In contrast, crystals work like 3D gratings including diffractions from their bulk. Fortunately, more than 100 different crystals are available [9], the particular spectral range of the application determines the most appropriate crystal, which ultimately depends on the spectral region to be measured. When choosing a crystal it's important to consider the crystal spacing (L), the diffraction efficiency of the diffraction order, lifetime of the crystal. For bent crystal spectrometers the flexibility of the material is important to a good design.

The conversion efficiency of laser light into X-rays is typically low; as a result the total number of photons to detect is low. Therefore to obtain single shot data an X-ray spectrograph must be very efficient. Crystals offer varying degrees of diffraction efficiency; it's possible to improve the photon flux onto the detector by bending the crystal such that it collects more photons and focuses them towards the detector plane. The Von Hamos spectrograph is one type

of curved crystal spectrograph where the crystal is cylindrically bent to increase the collection solid angle of plasma light while maintaining a high resolution dispersion plane that works very much like a flat crystal spectrometer [8, 9]. The bend is made along the polar angle of a cylinder where the plasma and detector plane are located along the axis of the cylinder, see the geometry in Figure 11. Care is made to align the bend with the axis of the crystal. In this scheme, X-rays are diffracted according to the Bragg diffraction equation,

$$m\lambda = 2d \sin\theta$$

where m, λ, d, θ are the diffraction order, the wavelength, the crystal lattice spacing and the angle of incidence, respectively.

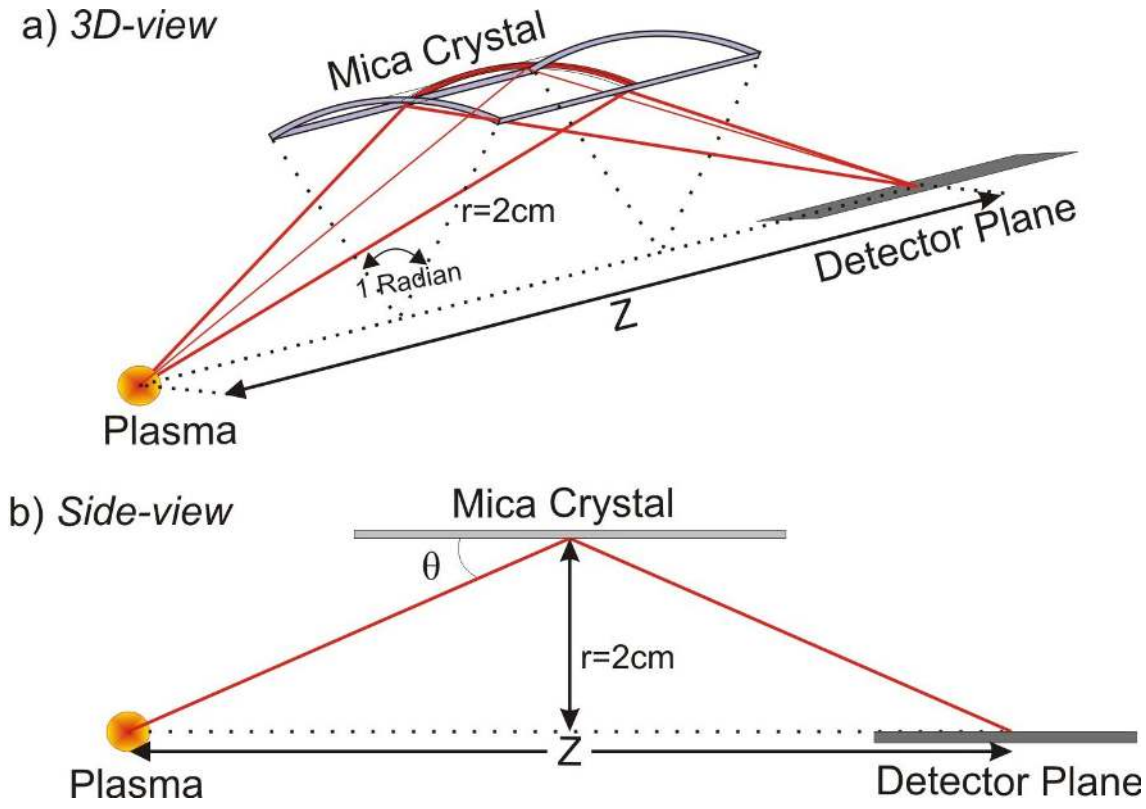

Figure 11. A schematic of the von Hamos X-ray spectrograph in a) 3D-view and b) side-view. Ray trace is shown in red.

Poor alignment of the plasma and the detector with respect to the axis of the curved crystal results in a distortion of wavelength dispersion along the detector plane and can cause a reduction in efficiency. These experiments utilized a MICA crystal that was chosen because of the high diffraction efficiency at 3rd order reflection for λ=1.4-2Å, λ=4.5-5.25 Å and at 1st order λ=6-11Å. Those wavelength regions are relevant to the highly ionized Nickel and Gold plasmas studied herein. The MICA crystal is easily bent to a radius of r = 2cm without having to apply special heating techniques necessary for bending many other crystals. A polar angle of 1 Radian was chosen for increased solid angle collection, more than this was not necessary as it becomes increasingly difficult to detect light at steep angles due to geometrical considerations. A photograph of the completed X-ray spectrograph is shown in Figure 12.

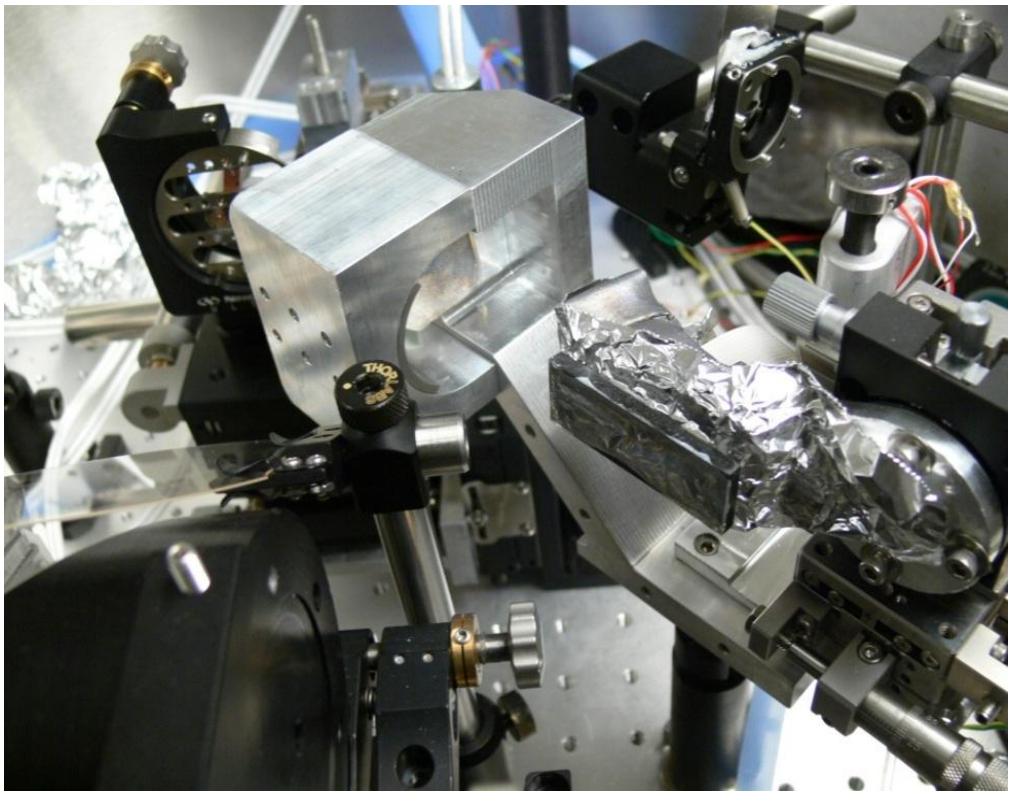

Figure 12. A photograph of the X-ray crystal spectrograph installed in the target chamber.

The detector consisted of a Si linear array CCD chip made by Toshiba, which was covered by filters chosen to attenuate out-of-band radiation from being detected. Lead foils, 1mm thick, were strategically placed to shield the electronics from the direct path of high energy particles.

In this geometry, wavelengths diffracted from the Bragg equation will lie at a distance Z from the plasma source, where Z is given by,

$$Z = \frac{2 \cdot r}{\tan \theta}$$

Wavelength calibration is performed for each geometrical arrangement. Calibration can be accomplished by geometry alone if the spectrograph is well aligned, first solving for Z as a function of wavelength, using the equation below.

$$Z = 2 \cdot r \cdot \cot\left(\sin^{-1} \frac{m\lambda}{2d}\right)$$

Alignment and the difficulty of precisely measuring the distance from the plasma to the detector position, present challenges to geometrical calibration. To help with this problem a pointing tool was developed to mechanically place the spectrometer a known distance from the plasma. A more precise calibration was performed fitting with the equation above a set of well- known spectral lines.

This device was first fielded by generating a Mg spectrum in the 7.5-10Å regime, see Figure 13. The calibration utilized 210ps pulses from a Ti:Sa laser with 120mJ of energy, focused to spot of ~10um FWHM on a flat optically polished Mg target. The Von Hamos spectrograph was setup in the 1st order diffraction of the Mica crystal, accomplished by correctly selecting the distance Z between the plasma and the detector plane. H-like and He-like Mg lines can be easily observed in Figure 13.

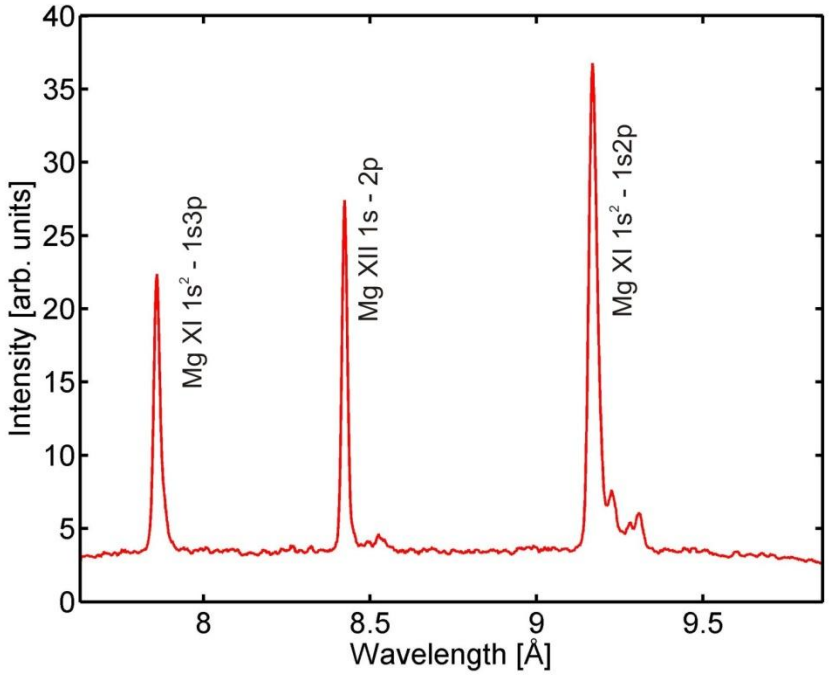

Figure 13. A single-shot Mg spectra acquired by the Von Hamos crystal spectrometer in the 7.5-10Å regime. The lines were utilized for initial wavelength calibration.

The calibration was found to be better than <0.01 Å across the full range of the detected wavelengths. The device was also efficient enough such that spectra could be obtained on a single shot when the CCD was covered with a filter consisting of a 1 μm of Mg deposited on a 3 μm Mylar film.

To calibrate spectra in the λ=1.5-1.75 Å region, a region of interest to He and Li charge states of ionized Ni plasmas, the Ni-Kα (λ=1.658 Å) line was used in combination with the Cu-Kα (λ=1.54 Å) from plasmas generated irradiating polished flat targets. In this arrangement, the spectrograph was aligned for distances corresponding to the m=1 order. Likewise, with only slight modifications the spectrograph could access the m=3 order, to observe the λ=4.5-5.25 Å wavelength region. In this case, diffraction efficiency was high enough to allow the same Ni and

Cu Kα lines (λ = 3*1.658 = 4.974 Å and λ = 3*1.54 = 4.62 Å) to be used for calibration in 3rd order reflection. Line identification of the Ni spectra was performed using data from the NIST Atomic Spectra Database **[11]**, while the Au spectra was identified primarily using the work from Busquet et al [12], complimented by data from May M.J et al. [13], and Scofield J.H. et al. [14].

2.3.2 The soft X-ray grating spectrometer

To monitor soft X-rays emitted by the plasma, the experiments utilized a slightly modified diffraction grating spectrometer, originally designed by Hettrick Scientific [15], where the entrance slit of the device was removed. The resolution of the device was practically unaffected by the modifications since the plasmas studied were on order of the width of the removed slit, <10μm in diameter. The spectrometer was positioned at a fixed polar angle of 30° from target normal (see Figure 10). The spectrometer has the capability of moving three different gold gratings into position, each with a different ruling, allowing a total accessible diagnosing range of λ =7-270Å. Soft X-rays were detected using a back-thinned 2D CCD array placed in the detection plane of the spectrometer and a Zr filter placed at the entrance was used to attenuate visible light.

The soft X-ray spectrometer was used to obtain preliminary results from Carbon nanowire arrays that revealed significantly enhanced production of light when compared to flat Carbon graphite targets.

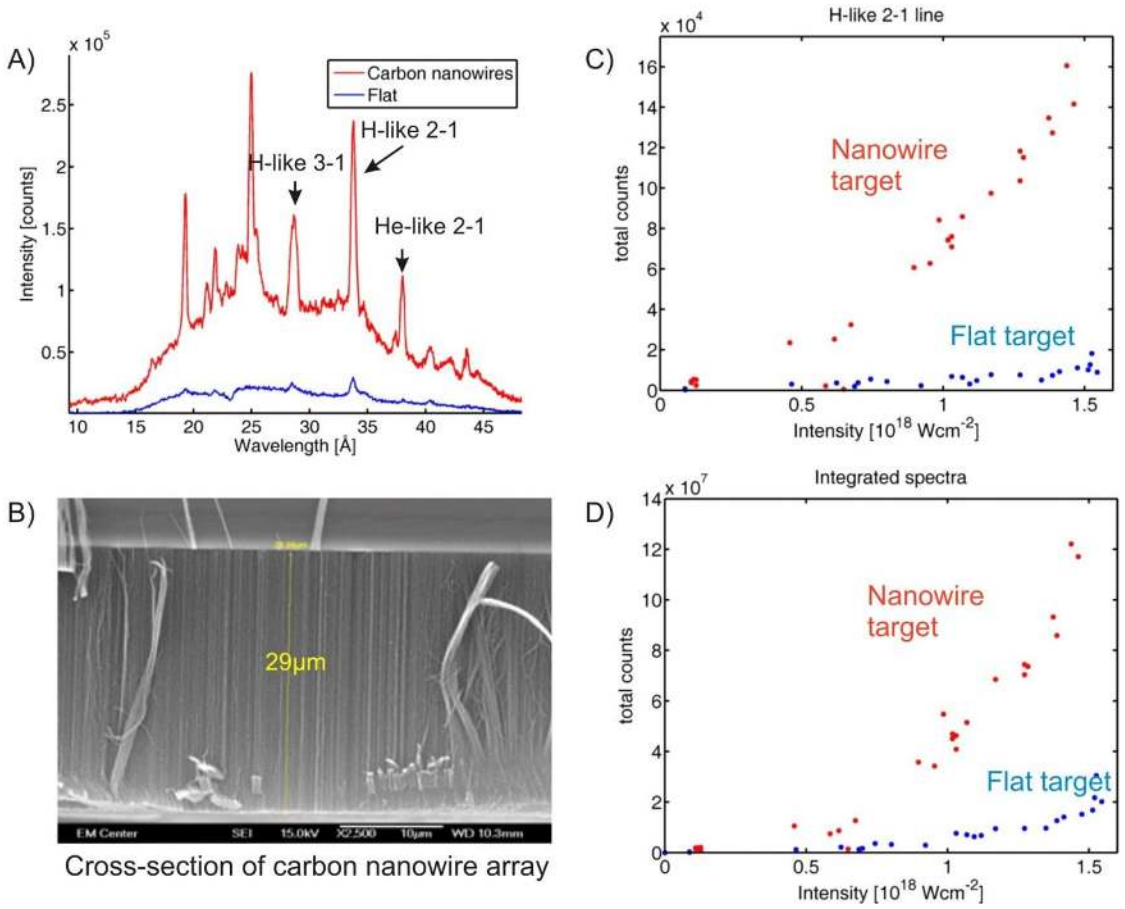

Figure 14. Soft X-ray results from vertically aligned Carbon nanowires irradiated by 350mJ pulses. A) Emission spectra obtained from laser irradiation of Carbon nanowires (red) that is compared to Carbon graphite (blue). B) SEM cross-section image of the nanowire array. Nanowires are 30nm in diameter and 29µm in length. C) A plot showing the H-like signal as a function of laser intensity for the nanowire array (red) compared to the graphite target (blue). A rapid increase in H-like production from the nanowire array can be observed as the laser intensity is increased beyond $5x10^{17}$ Wcm^{-2} D) The total integrated emission in the band of 15-45nm as a function of laser intensity.

Figure 14 (A), shows an example of a single-shot soft X-ray spectra obtained irradiating an array of vertically aligned Carbon nanowires with the output of a high contrast frequency doubled Ti:Sapphire laser. When compared to the radiation from a flat carbon graphite target, the nanowire arrays produce more than 20X the integrated soft X-ray emission with far brighter observed characteristic line emission. The total soft X-ray emission was seen to increase non-linearly with pulse intensity. Specifically, the H-like 2p-1s signal increases at a faster rate for the

nano-wire array than the flat target. The results agree with similar observations previously seen studying vertically aligned Carbon nanowire arrays [16].

A similar spectra, shown in Figure 15, was obtained in the 7-20 Å range for Ni, where a 20 fold increase in emission from the nanowire target was observed in the soft X-ray spectral region around 1 keV. The emission from 15µm long Ni nanowires 55nm diameter were compared to the emission from a polished flat Ni target irradiated with λ=400nm laser pulses of ~350mJ of energy at an intensity of $1x10^{18}$ W cm^{-2}. These are the shortest wavelengths we were able to observe with the grating spectrometer, since the reflectivity of gold at 2° grazing incidence quickly drops off at around 6 Å. A large group of Oxygen-like and Fluorine-like lines was assigned to the bump in the spectra spanning the 11-13 Å spectral region. The Ni nanowire target integrated soft x-ray emission in the band 6-20nm produced ~20X more light than the flat solid slab target.

2.3.3 The photodiode array

Angular emission profiles and time integrated radiation yields were obtained using an array of up to 12 filtered Si diodes (AXUV100G OptoDiodeCorp). These diodes are highly sensitive and have a linear response over 7 orders of magnitude. The spectral sensitivity covers visible to hard X-ray emission, 0.6-12keV. Throughout this energy range the quantum efficiency of the photodiodes is linear, QE=Ephoton/3.65eV. The energy emitted isotropically in 4πSr can be calculated using the following equation:

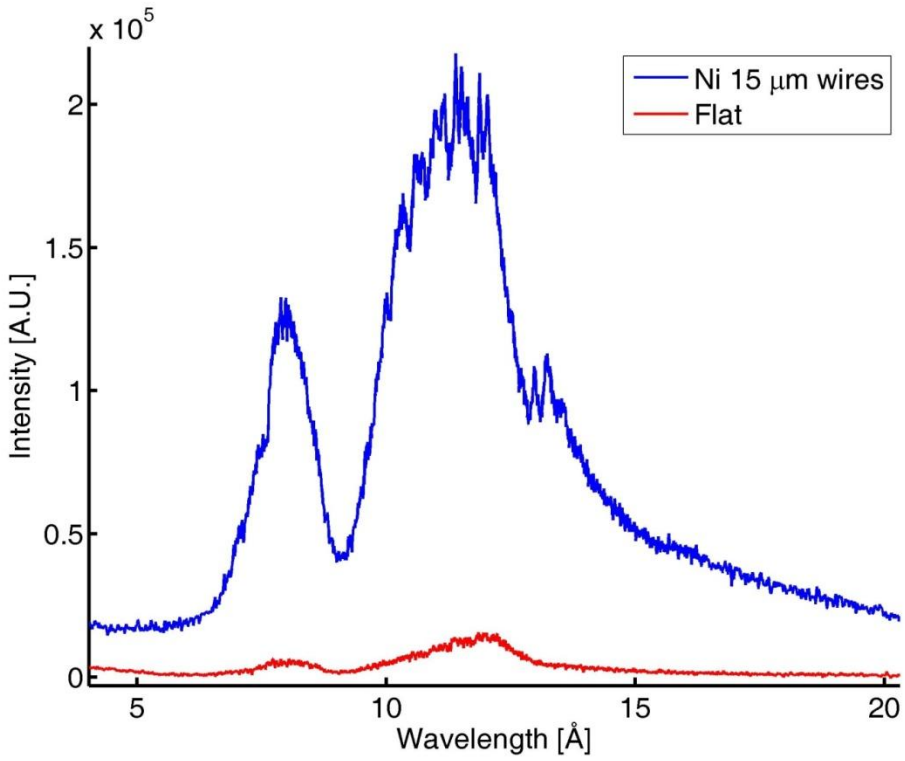

Figure 15. Time-integrated soft X-ray spectra in the range of 7-20Å region comparing the emission from 55nm diameter, 15μm long, Ni wires to that from a polished flat Ni target. The nanowire target emits 20X more X-rays in the ~1 KeV spectral region.

$$E(J) = \frac{3.65}{0.98}\frac{4\pi L^2}{A_{PD}}Q$$

Where L is the distance from the plasma to the photodiode, A_{PD} is the area of the photodiode exposed to radiation and Q is the charge produced by the diode. Charge is found by post processing the diodes scope traces using the following relationship.

$$Q = \frac{1}{Gain}\int V dt$$

where V is the oscilloscope voltage. The Gain is a measured value that is provided by injecting a known signal into the diode amplifier circuit. The experiments described herein did not have to rely on an assumption of isotropic emission into 4pi Sr or 2pi Sr. Instead, each diode was

processed independently to obtain Energy [mJ/Sr], providing information on the directional distribution of emission.

An example of the raw voltage signals simultaneously acquired from a set of 8 diodes is shown below.

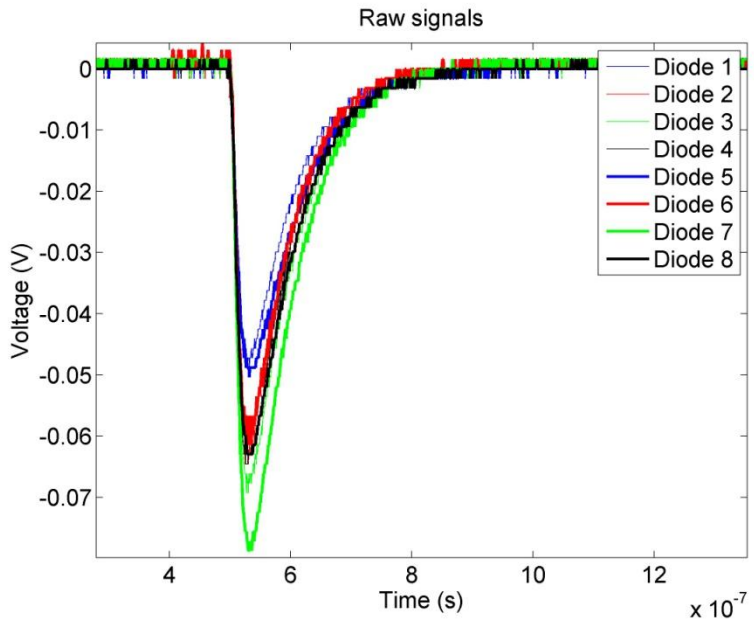

Figure 16. Example of a typical scope trace from the filtered photodiode array. These scope signals are integrated to obtain charge produced by the diode that relates to the energy generated by the plasma within the filtered band.

Each diode was housed in a miniature electrically grounded faraday cage with double shielded coaxial cables designed to shield the device from radio frequency noise emitted by the plasma. The diode assemblies were mounted at equally spaced polar angles on a circular rail with a radius of 28cm, centered at the laser focus. All diode signals were captured for every shot using three triggered oscilloscopes with 4 channels on each oscilloscope, allowing the direction of X-ray emission as a function of polar angle to be captured on a single-shot basis with 12 filtered diodes.

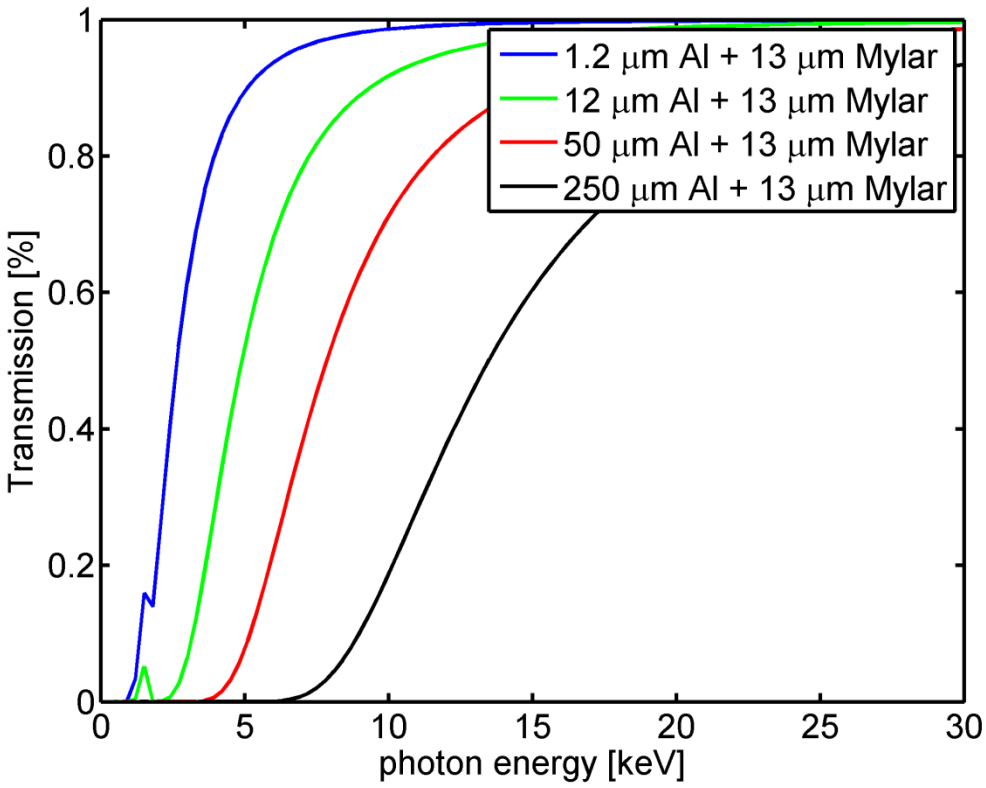

Figure 17. Transmission curves as a function of photon energy of the filter sets placed in front of the photo diodes. The filters consisted of a thin Al foils of different thickness placed on top of a 13 μm Mylar sheet.

Four sets of high-pass transmission filters were used throughout the experiments to measure the plasma angular X-ray emission pattern in different spectral regions. Filter sets consisted of a 13 μm of Mylar film combined with Aluminum foils with a thicknesses of, 1.2μm Al, 12μm Al, 50μm Al, or 250μm. These high-pass filters allow for the measurement of radiation from spectral regions defined by 15% transmission at: >0.9, >3.5, >5.6 and >9 keV. The reported conversion efficiencies (CE) of laser energy to X-ray production were obtained by accounting for the filter transmission and the anisotropy of the emission profile.

References

1. Prieto A.L. et al. Electrodeposition of Ordered Bi2Te3 Nanowire Arrays. *J. Am. Chem. Soc.*, **123**, 7160-7161 (2001).
2. Synkera Technologies Inc. http://www.synkerainc.com/ (2013).
3. Zaraska L., Sulka G.D., Jaskula M. Fabrication of free-standing copper foils covered with free-standing copper nanowire arrays. *Appl. Surf. Sci*, (2012).
4. Spence D.E., Kean P. N., and Sibbett W. 60-fsec pulse generation from a self-mode-locked Ti:sapphire laser, *Opt. Lett*., **16** 42-44 (1991).
5. DeLong K. W., Trebino R. and Kane D. J. Comparison of ultrashort-pulse frequency-resolved-optical-gating traces for three common beam geometries, *Opt. Soc. Am.* B **11** 1595 (1994).
6. Trebino R, DeLong K. W., Fittinghoff D. N., Sweetser J. N., Krumbügel M. A., and Kane D. J., Measuring Ultrashort Laser Pulses in the Time-Frequency Domain Using Frequency-Resolved Optical Gating, *Rev. Sci. Inst.* **68**, 3277-3295 (1997).
7. Sweester J. N., Fittinghoff, D.N. and Trebino R., Transient-grating frequency-resolved optical gating, *Opt. Lett*., **22**, 519-521 (1997).
8. Hamos L.V. Von, Rontgenspektroskipie und Abbildung mittels gekrummter Kristallreflektroren, Ann. Phys. 17 716-724 (1933).
9. X-ray data booklet, Lawrence Berkeley National Lab, University of California, http://xdb.lbl.gov/ (2009).
10. Shevelko, A. P., Kasyanov, Yu. S., Yakushev, O. F. & Knight, L. V. Compact focusing von Hamos spectrometer for quantitative X-ray spectroscopy. *Rev. Sci. Instrum.*, **73**, 3458-3463 (2002).
11. Kramida, A., Ralchenko, Yu., Reader, J. and NIST ASD Team (2013). NIST Atomic Spectra Database (version 5.1), [Online]. Available: http://physics.nist.gov/asd [Tuesday, 15-Apr-2014 19:22:43 EDT]. National Institute of Standards and Technology, Gaithersburg, MD.

12. Busquet M., Pain D., Bauche J., Luc-Koenig E. Study of X-ray Spectrum of Laser-produced Au Plasmas, *Physica Scripta*, **31**, 137-148 (1985).
13. May, M. J., Fournier, K. B., Beiersdorfer, P., Chen, H. & Wong, K. L. X-ray spectral measurements and collisional radiative modeling of Ni- to Kr-like Au ions in electron beam ion trap plasmas. *Phys. Rev. E.*, **68**, 1-11 (2003).
14. Scofield, J.H., & Kauffman, R. X-ray radiation from laser plasma, *Physics of Laser Plasma* (1991).
15. Hettrick Scientific http://www.hettrickscientific.com/ (2013).
16. Nishikawa T., Suzuki S., Watanabe Y., Zhou O., Nakano H. Efficient water-window X-ray pulse generation from femtosecond-laser-produced plasma by using a carbon nanotube target. *Appl. Phys. B*, **78**, 885-890 (2004).

Chapter 3: The generation of ultra-hot-dense plasmas

3.1 Introduction

Here I show results from the first demonstration of volumetric heating of near-solid density plasmas to keV temperatures using ultra-high contrast femtosecond laser pulses of only 0.5 J energy to irradiate arrays of vertically aligned nanowires. Our X-ray spectra and particle-in-cell (PIC) simulations show extremely highly ionized plasma volumes several micrometers in depth are generated by irradiation of Au and Ni nanowire arrays with femtosecond laser pulses of relativistic intensities. This volumetric plasma heating approach creates a new laboratory plasma regime in which unprecedented plasma parameters can be accessed with table-top lasers. The increased hydrodynamic-to-radiative lifetime ratio is responsible for a dramatic increase in the X-ray emission with respect to polished solid targets.

3.2 Simulations and Experimental Results

PIC simulations were conducted with the fully electromagnetic particle-in-cell code VLPL (virtual laser-plasma laboratory)[1]. The full three dimensional geometry was used. We assumed Ni nanowires of 55 nm diameter arranged in an array with the periodicity of 135 nm. The laser pulse was modeled by a plane wave with the time envelope $a(t) = a_0 \exp\left(-t^2/\tau^2\right)$ where the relativistic amplitude $a_0 = eA/mc^2 = 0.75$ corresponds to the laser intensity of $I_0 = 4.8 \cdot 10^{18}$ W/cm^2 and the pulse duration $\tau = 40\,\text{fs}$ (60 fs FWHM) impinging at normal incidence on the nanowire array. The standard PIC algorithm was extended by packages for optical field ionization (OFI), binary collisions, and electron impact ionization. The OFI was treated as an under barrier tunneling in the static electric field [2, 3]. Only sequential field

ionization is considered. The binary collisional package calculated probabilities of Coulomb collisions between all particles in one mesh cell. The code was run on 256 processors of a local Intel-Nehalem cluster.

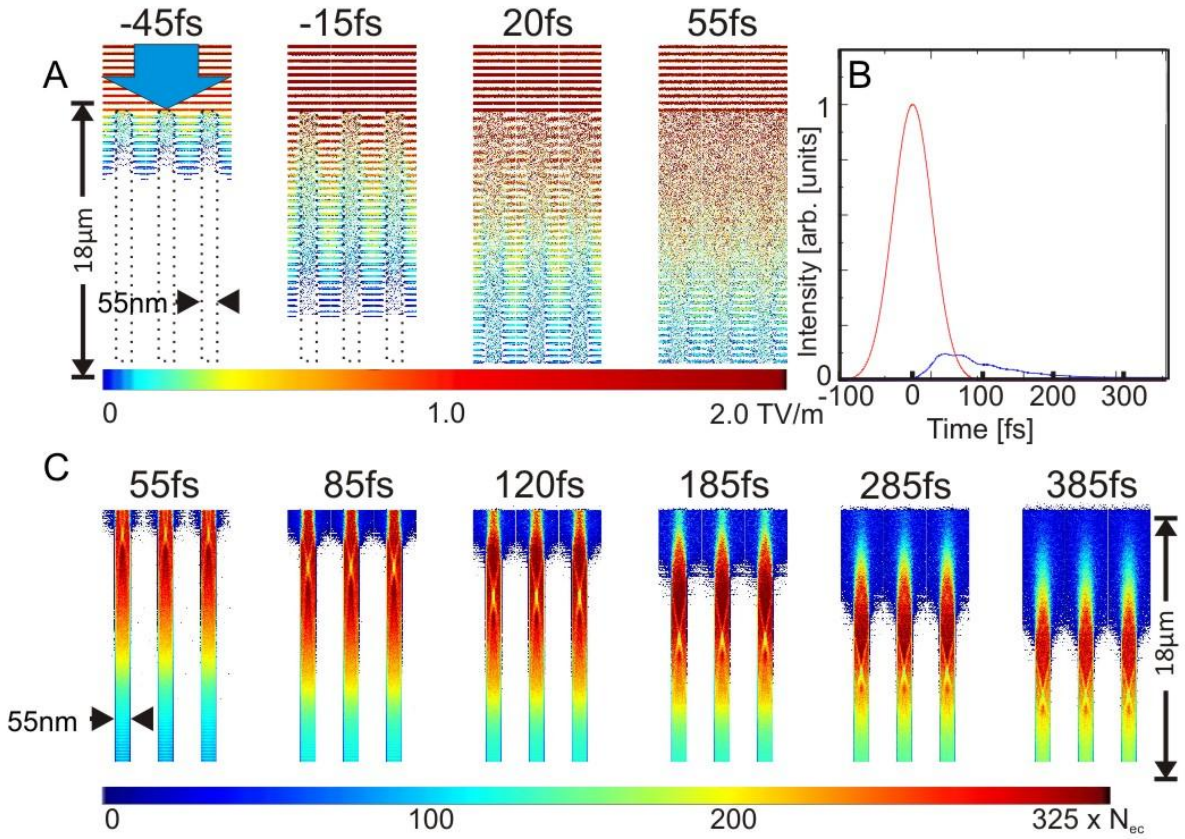

Figure 18. Particle-in-cell simulation and spectra from plasma generated by femtosecond pulse irradiation of a vertically aligned array of 55 nm diameter Ni nanowires. (A) PIC simulations of the penetration of the laser beam electric field in an array of 18 µm long Ni wires with an average atomic density of 12% solid density irradiated at an intensity of 5 x 10 ^{18} W cm^{-2} by a λ= 400 nm, 60 fs FWHM duration laser pulse. Times are measured with respect to the peak of the laser pulse. The laser field scale is in units of TV/m. (B) Computed impinging (red contour) and reflected (blue contour) laser intensity. (C) Computed electron density evolution. The electron density scale is units of critical density (N_{ec}=6.8x10^{21} cm^{-3}).

The sequence of PIC maps in Fig.18 A shows that an intense femtosecond laser pulse can penetrate deeply into an array of vertically aligned Ni wires 55 nm diameter where is nearly totally absorbed (Fig.18B). The simulation describes all the phases of nanowire heating, explosion, and volume plasma formation. Local field enhancement [4], field fluctuations, and resonance heating [5], are all described by the code. However, since the average density is much higher than the critical density and the nanowire spacing is much smaller than the laser wavelength, bulk resonances are not present. Optical field ionization is active at the boundary of the nanowires where vacuum heating of electrons takes place [5]. The hot electron population drives collisional electron impact ionization deep into the nanowire core (OFI is insufficient to ionize beyond Z=18), causing the plasma to rapidly reach an electron density of $2x10^{24}$ cm^{-3} (left frames in Fig.18C). Despite the high average electron density, the laser pulse propagates deeply inside the nanostructured material as long as the gaps between the nanowires are free from plasma. Free electrons inside the nanorods are bound by collective fields and do not contribute to the plasma refractive index. The high energy deposited into the nanowire cores is transformed into a thermal energy density of ~ 2 $GJcm^{-3}$, with average thermalized electron energy of 4 keV over the penetration depth and ~ 8 keV near the nanowire tips. The heated nanowire plasmas rapidly expand radially until the plasma fills the vacuum gaps. Beyond this point any further propagation of laser light deep into the target is effectively terminated by the formation of a critical density surface. The ultra-short duration of the laser pulse allows for the majority of the energy to be efficiently deposited before the gap closure. The hot plasma formation starts at the tip of the wire and propagates along the wires towards the supporting substrate (Fig.18C). Our simulations show that 350 fs after the peak of laser irradiation a fiber length of 4-5 μm has "burned" (Fig.18C), creating a plasma layer with an average density of $3x10^{23}$ cm^{-3} and an

electron temperature of 2-4 keV, in which an extremely high degree of ionization is rapidly reached by collisional electron impact ionization.

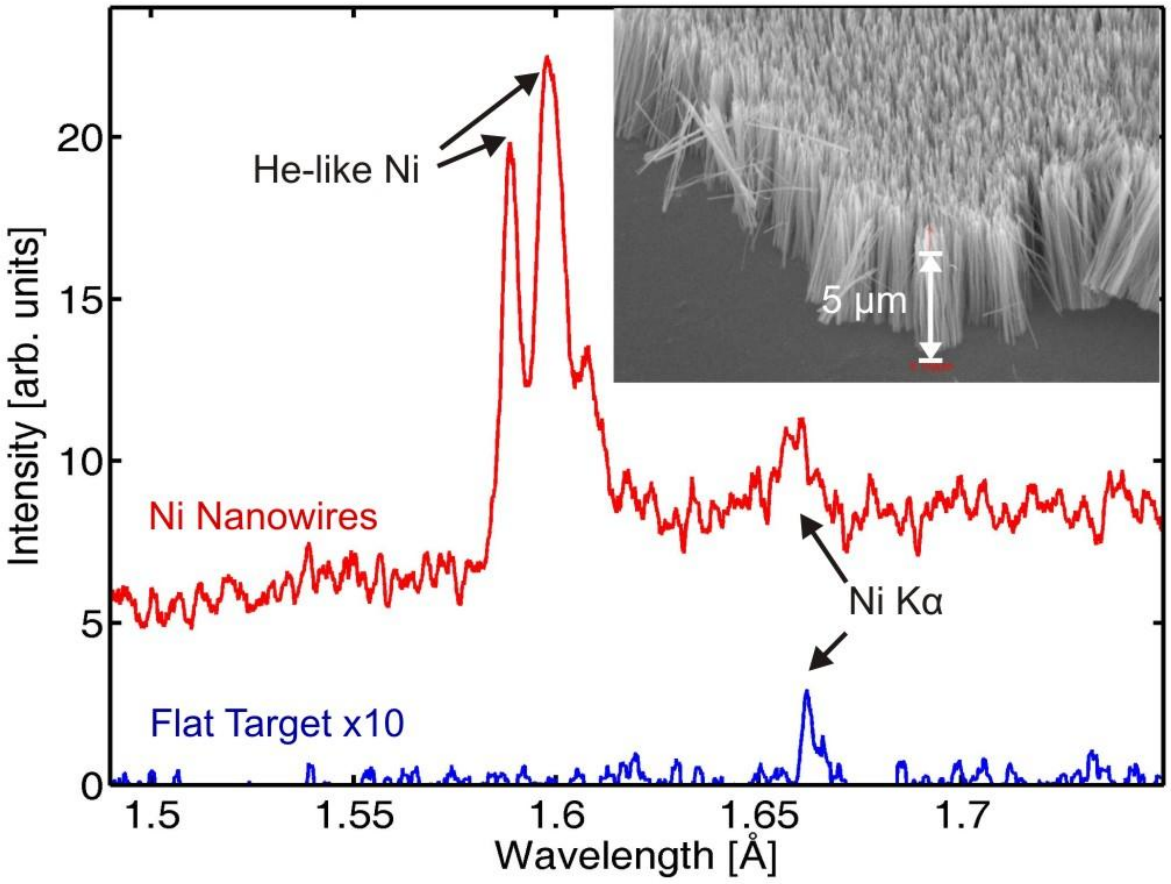

Figure 19. Single-shot X-ray spectra comparing the emission from an irradiated array of 5 μm long, 55nm diameter, Ni nanowires to that from a flat polished Ni target. The nanowire target plasma spectra is dominated by He-like Ni resonance and intercombination line emission. The latter is merged with several $1s2p^2$ -$1s^22p$ lines from Li-like Ni. The only line observed in the flat target plasma spectra is the Ni-Kα line. The inset is an scanning electron microscope image of the array of vertically aligned nanowires.

Figure 19 shows a single-shot spectrum of the emission in the 1.5-1.75 Å region for a plasma created from vertically aligned Ni nanowires 55 nm diameter separated by 135 nm. Strong emission from the 2p-1s (λ=1.588 Å) and intercombination lines of He-like Ni (Ni^{+26}) is

observed, the latter merged with Li-like Ni lines. This spectrum differs dramatically from that corresponding to a polished flat target irradiated at the same conditions which only shows line emission from the Ni Kα line at 1.658 Å (with 10 X magnified scale in Fig.19). The Kα emission is produced mainly by high energy electrons, while generation of the He-like ion transitions requires a hot thermal plasma to generate and excite the highly stripped ions. It is remarkable that the He-like line emission from the nanowire target exceeds the intensity of the Kα line at this irradiation intensity, since in previous work with Cu foils the emission from the Kα lines was only surpassed at irradiation intensities > $2x10^{20}$ Wcm^{-2} [6]. The aligned Ni nanowire target produced an increase of more than 50 times in X-ray flux in this 7-8 keV spectral region. Similar enhancements were also observed in the 1 keV photon energy region in agreement with previous experiments [7].

Similarly, a near solid-density Au plasma with an extraordinarily high degree of ionization was created by irradiating an array of 80 nm diameter Au wires 5 μm in length. The Au nanowire spectrum in Fig.20 (λ=4.5-5.25 Å region) displays strong Au M-shell emission with unresolved 4-3 lines from ions ranging from Co-like (Au^{+52}) to Ga-like Au (Au^{+48}) [8]. Both the spectra and the filtered photodiode array signals from the Au targets show a dramatic increase in X-ray yield with respect to flat solid targets irradiated by the same pulse. The spectra show increases of up to 100X in the emission in the 2.3 keV to 2.75 keV photon regions. Filtered photodiode measurements show a 50X emission increase for photon energies > 8 keV. Spectra obtained for arrays of 35 nm and 80 nm diameter nanowires also display strong He-like line emission, in agreement with the prediction of PIC simulation.

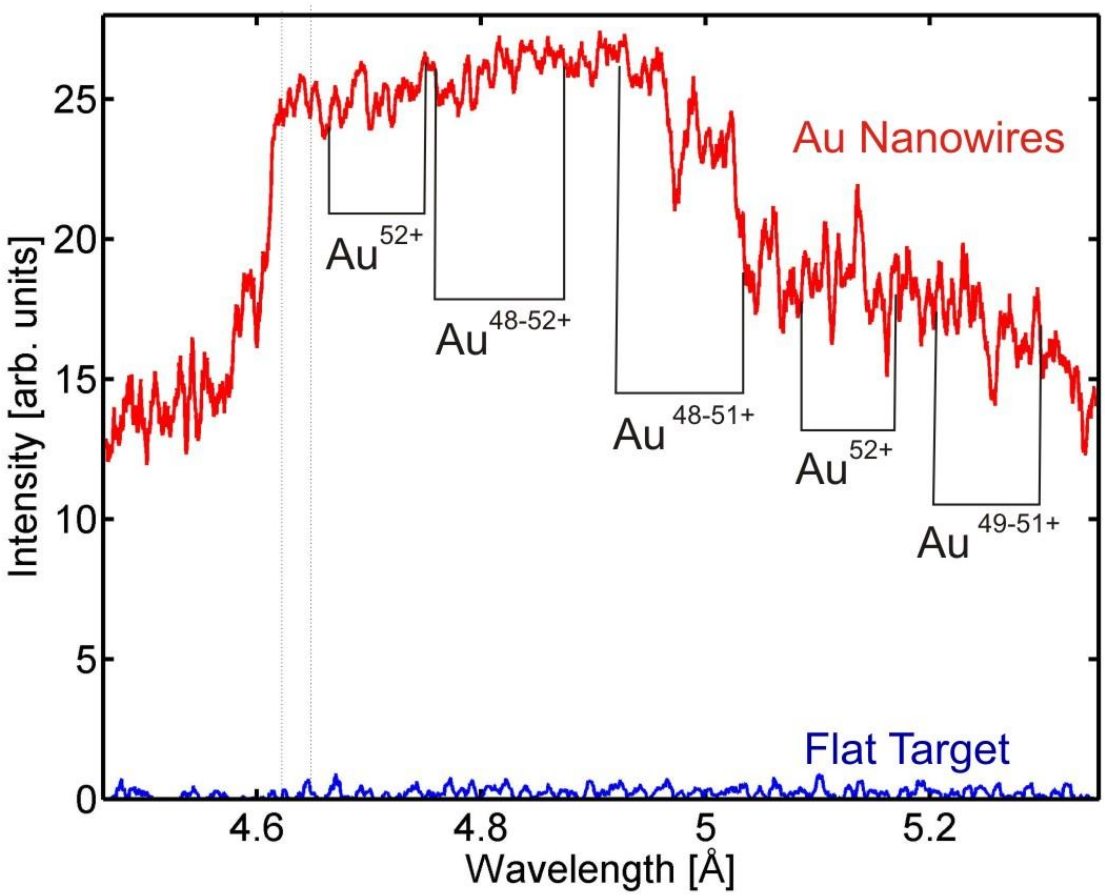

Figure 20. Single shot M-shell spectra of vertically aligned arrays of 80 nm diameter Au nanowires compared with the spectra from a flat polished Au target. The target is Irradiated at an intensity of 5x 10^{18} W cm^{-2} with a high contrast λ=400 nm wavelength laser pulse of 60 fs FWHM duration. Brackets highlight regions where the emission is dominated by Co-like, Ni-like, Cu-like, Zn-like, and Ga-like Au ions. The dashed line defines the region where there is a contribution from the K-α line of Cu that originates from a copper layer at the base of the Au nanowires.

The depth to which the Ni nanowire target is ionized to the He-like state was experimentally determined to be 3-4 μm by monitoring the spectrally resolved X-ray emission as a function of nanowire length. Figure 21B shows spectra from arrays of 55 nm diameter Ni nanowires of four different lengths between 1 μm and 12.5 μm. The intensity of the He-like line is observed to

increase with nanowire length until it saturates for a length of about 4 μm, beyond which it remains virtually unchanged. In contrast, the K-α emission continues to increase beyond this length as the fast electrons interact with a larger volume of neutral atoms. The PIC simulations reproduce the experimental results in showing a plasma depth of several μm is volumetrically heated to reach the He-like ion stage. Figure 21A shows that 385 fs after the peak of the irradiation pulse a plasma depth of ~ 5 μm is computed to be ionized to the He-like stage. This large increase in heated plasma volume relative to plasmas from flat solid targets irradiated at the same conditions significantly lengthens the plasma hydrodynamic time. Simultaneously, the radiative lifetime is greatly decreased as a result of the nearly two orders of magnitude increase in plasma density, the higher temperature, and higher average Z of the nanowire plasma. The combination of these two effects results in a greatly decreased cooling-time to hydrodynamic-time ratio, a key parameter governing the X-ray conversion efficiency. This and the increase in plasma density explain the dramatic increase in the X-ray yield observed in nanowire plasma experiments.

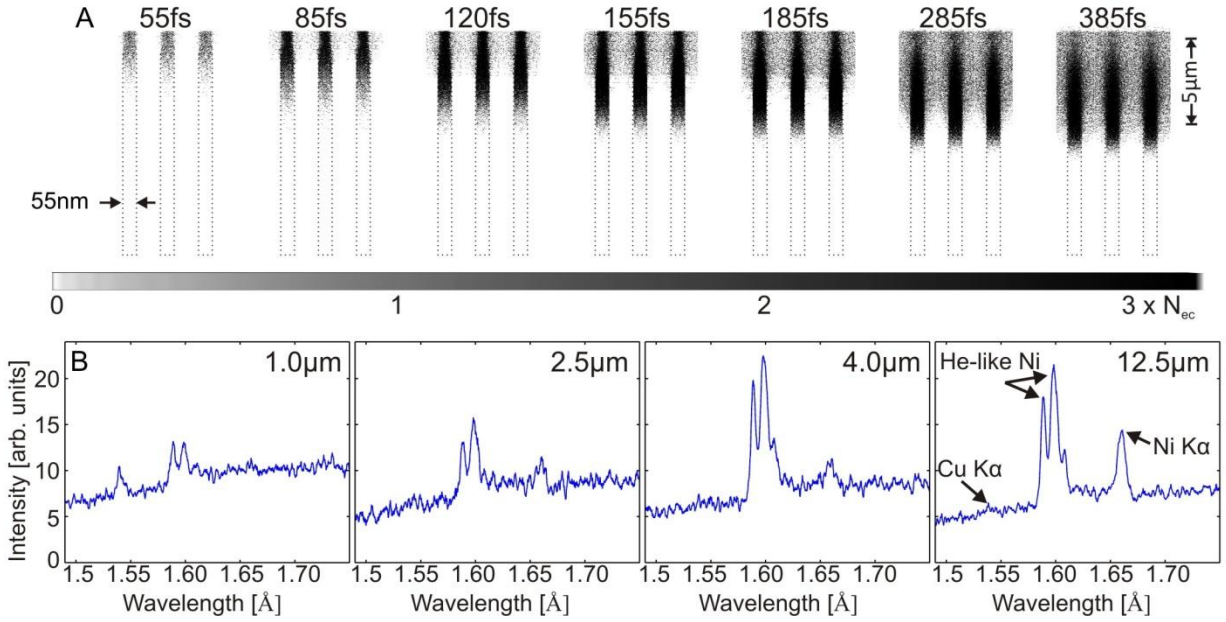

Figure 21. Generation of He-like ions in the volumetrically heated Ni plasmas. (A) Particle-in-cell simulation maps showing the evolution of the density of He-like nickel ions. The He-like ion density is in units of critical electron density (N_{ec}= $6.8x10^{21}$ cm^{-3}). The wires are 55 nm diameter, and the array has an average atom density of 0.12 solid. The irradiation intensity is $5x10^{18}$ W cm^{-2}. (B) X-ray emission of nanowire targets of four different lengths: 1, 2.5, 4, and 12.5 μm. Heα emission is observed to saturate for wire lengths > 4 μm, suggesting a plasma volume 3-4 μm deep is heated sufficiently for ionization to reach the He-like stage.

3.3 Discussion

Other plasma parameters are computed to be exceptional: the wire core is calculated to reach thermal pressures of 10 Gbar and a thermal energy density of 2 $GJcm^{-3}$, while the plasma created after the dissolved wires expand, collide, and thermalize, is computed to have a thermal energy density of 0.3 $GJcm^{-3}$ and a pressure of 1-2 Gbar. This pressure is nearly two orders of magnitude larger than that in inertial confinement fusion hohlraum plasmas [9] and is comparable to that created in the central hot-spot of the imploded fusion capsule in the early

National Ignition Facility (NIF) experiments at ultra-high laser energy[4]. The nanowire plasma conditions are surpassed only by those obtained when the NIF capsule is highly compressed[3], effectively creating an new laboratory plasma regime (Chapter 1 Fig. 5). Furthermore, our simulations predict that irradiation of vertically aligned nano-photonic arrays with highly relativistic intensities will reach unprecedented degrees of ionization in dense laboratory plasmas. For example, irradiation of a uranium nanowire array with laser intensities of $1x10^{20}$ Wcm^{-3} can be expected to generate plasma densities of $1x10^{24}$ cm^{-3} dominated by >70 times ionized atoms.

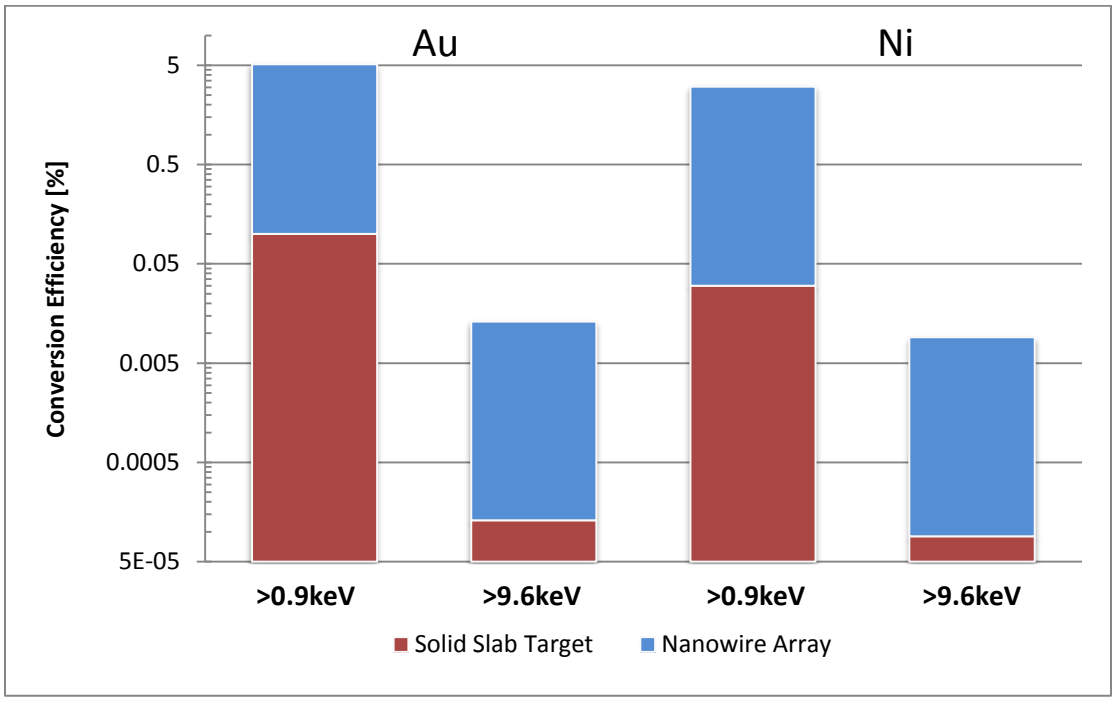

Figure 22. Measured conversion efficiency results obtained irradiating nanowire arrays and solid flat polished slab targets at intensities of $5x10^{18}$ W cm^{-2}.

A consequence of producing volumetrically heated, near solid-density plasmas is the efficient production of X-ray and soft X-ray emission. Record conversion efficiencies were observed with the diode array for Au nanowires 55nm diameter and a 12% average density of nanowires. A

conversion efficiency of >5% in 2π Sr for photons with energies >0.9keV and >1.3% for photons with energies >9.6keV was measured, see Fig. 22. The Au nanowire array produced ~2X more emission than Ni. The emission for photons >0.9keV was more than 100X over the emission of polished flat targets irradiated under the same conditions. Similar large enhancements in emission were confirmed using the von Hamos x-ray spectrometer, although the dynamic range was limited by the CCD to ~50X and therefore it was unable to fully resolve the large differences in emission between flat and nanowire targets.

References

1. Pukhov A. Three-dimensional electromagnetic relativistic particle-in-cell code VLPL (Virtual Laser Plasma Lab). *Journal of Plasma Physics,* **61**, 425-433 (1999).
2. Zhidkov A., Sasaki A. Effect of field ionization on interaction of an intense subpicosecond laser pulse with foils. *Physics of Plasmas*, **7**, 1341-1344 (2000).
3. Karmakar A., Pukhov A. Collimated attosecond GeV electron bunches from ionization of high-Z material by radially polarized ultra-relativistic laser pulses. *Laser and Particle Beams,* **25**, 371-377 (2007).
4. Mondal S. et al. Highly enhanced hard x-ray emission from oriented metal nanorod arrays excited by intense femtosecond laser pulses. *Phys. Rev. B*, **83**, 035408 (2011).
5. Brunel F. Not-so-resonant, resonant absorption. *Phys. Rev. Lett*., **59**, 52-55 (1987).
6. Theobald W. et al. Hot surface ionic line emission and cold K-inner shell emission from petawatt-laser-irradiated Cu foil targets. *Phys. Plasmas* **13**, 043102 (2006).
7. Kulcsár G. et al. Intense Picosecond X-Ray Pulses from Laser Plasmas by Use of Nanostructured “Velvet” Targets. *Phys. Rev. Lett.*, **84**, 5149-5152 (2000).
8. Busquet M., Pain D., Bauche J., Luc-Koenig E. Study of X-ray Spectrum of Laser-produced Au Plasmas, *Physica Scripta*, **31**, 137-148 (1985).
9. MacGowan B.J. et al. Laser-plasma interactions in ignition scale hohlraum plasmas. *Phys. Plasmas*. **3**, 2029-2040 (1996).

Chapter 4: Discussion

The propagation of femtosecond duration high-contrast laser pulses with intensities of $5x10^{18}$ Wcm^{-2} traveling deep (several micrometers) within arrays of ordered, nanowires was demonstrated to create volumetrically heated plasmas with an extreme degree of ionization. The laser pulse heats a volume of near-solid density material, generating highly ionized plasma with densities and a degree of ionization that far exceeds what can be produced by irradiation of a solid slab target. The nanowire array offers a means to overcome the limitation of the critical density surface, providing access to a new regime of ultra-high energy density plasmas, using femtosecond duration pulses of only 0.5 Joules. Simulations performed with a 2D particle in-cell code revealed the evolution of the heated wires, showing that the plasma is first formed near the tips of the wires and propagates towards the base of the wires, filling the gaps between the individual wires with dense plasma. Pressures of 1-2 Gbar were computed within the nanowire core, that agree well with experimental findings of plasma ionization and conversion efficiency. Measurements from a bent crystal X-ray spectrometer reveal Ni atoms in nanowires plasmas were ionized up to 26 times and Au atoms were ionized up to 52 times. Monitoring the He-α line strength while varying the nanowire length revealed a heated volume with a depth of ~3-4μm, composed of a near-solid density plasma. Conditions where the radiative cooling time to hydrodynamic time ratio is large were created, which are ideal for the production of X-rays. Measurements with a filtered photodiode array yielded a conversion efficiency of more than 5% into photons with energy >0.9keV.

4.1 Future investigations

There are many possibilities to take this investigation further. For example, studies at higher intensities promise to create some of the world's highest degree of ionization and laser-produced plasma pressures. For example, irradiation of an uranium nanowire array at an intensity of 1 $x10^{20}$ cm^{-2} is predicted to create plasmas with an electron density of 1 x 10^{24} cm^{-3} with atoms ionized > 70 times. Many currently available lasers are capable of reaching this intensity and beyond. It is of interest to further increase conversion efficiency and extend the results into harder X-rays (>20keV). Further studies are necessary to fully understand that plasma heating and X-ray generation mechanisms. In recent preliminary measurements we have observed that the emission of hard X-rays (hv> 10 KeV) is not isotropic. The use of distributed arrays of diodes will be useful to measure the dependence of X-ray emission on angle, and to understand the role that hot electrons play in producing X-ray emission. Parametric studies of nanowire geometry vs. laser pulse characteristics are also of interest to the optimization of X-ray yield. Time resolved diagnostics can also contribute to a better understanding that can ultimately result in an increased X-ray yield.

LETTERS
PUBLISHED ONLINE: 1 SEPTEMBER 2013 | DOI: 10.1038/NPHOTON.2013.217

nature photonics

Relativistic plasma nanophotonics for ultrahigh energy density physics

Michael A. Purvis[1], Vyacheslav N. Shlyaptsev[1], Reed Hollinger[1], Clayton Bargsten[1], Alexander Pukhov[2], Amy Prieto[3], Yong Wang[1], Bradley M. Luther[1,3], Liang Yin[1], Shoujun Wang[1] and Jorge J. Rocca[1,4]*

The heating of dense matter to extreme temperatures motivates the development of powerful lasers[1–4]. However, the barrier the critical electron density imposes to light penetration into ionized materials results in the deposition of most of the laser energy into a thin surface layer at typically only 0.1% of solid density. Here, we demonstrate that trapping of femtosecond laser pulses of relativistic intensity deep within ordered nanowire arrays can volumetrically heat dense matter into a new ultrahot plasma regime. Electron densities nearly 100 times greater than the typical critical density and multi-keV temperatures are achieved using laser pulses of only 0.5 J energy. We obtained extraordinarily high degrees of ionization (for example, 52 times ionized Au) and gigabar pressures only exceeded in the central hot spot of highly compressed thermonuclear fusion plasmas. Scaling to higher laser intensities promises to create plasmas with temperatures and pressures approaching those in the centre of the Sun.

Long-lived plasmas that are simultaneously dense and hot (multi-keV) have been created by spherical compression in fusion experiments at the world's largest laser facilities and by supersonic heating of volumes with densities on the order of the critical electron density N_{ec} using multi-kilojoule laser pulses[1–4]. Such high-energy laser pulses have ionized mid-atomic number (Z) plasmas to the He-like and H-like stages[5,6] and have stripped high-Z elements such as Au to charge states neighbouring the Ni-like ion[6–8]. Supersonic thermal conduction on a timescale faster than hydrodynamic expansion and strong shock waves driven by high-intensity ultrashort pulse lasers can also create very hot near solid density plasmas[9]. However, due to the relatively slow speed of the shock wave, the region with both high temperature and high density is narrow, typically ~0.1 μm (refs 9,10). Petawatt laser irradiation of Cu foils with 0.7-ps-duration laser pulses has generated thin surface plasma layers with electron temperatures of 2–3 keV in which the Cu He-α line intensity exceeds that of the Cu k_α line[11]. Recently, high-contrast laser pulses from a petawatt laser were reported to heat a plastic target at a depth of 30 μm to an electron temperature of 600 eV (ref. 12). Experiments with lower density targets have also produced volumetrically heated plasmas with high temperatures. Heating of 10% solid density Cu foams with a 0.93 kJ pulse has produced 1.5 times greater He-like line emission than a Cu foil[13]. Irradiation of clusters has been shown to create plasmas with multi-keV electrons and extremely energetic ions, but with only moderate average densities[14]. In turn, experiments that monitored the X-ray emission from plasmas that created irradiating structured targets[15–18], 'smoked' targets[19,20] and nanowire arrays[20–23] have shown large increases in X-ray flux, suggesting the formation of a hot dense plasma and/or enhanced hot electron production. In particular, the irradiation of arrays of 0.8- to 1-μm-long Ni nanowires with picosecond laser pulses has produced up to 50 times greater emission than a flat target in the ~1 keV photon region[20], and irradiation of Au nanowire arrays produced a 20-fold increase in soft X-ray emission[23].

Here, we demonstrate, for the first time, the volumetric heating of near-solid density plasmas to keV temperatures using ultrahigh-contrast femtosecond laser pulses of only 0.5 J energy to irradiate arrays of vertically aligned nanowires. Our X-ray spectra and particle-in-cell (PIC) simulations show that extremely highly ionized plasma volumes several micrometres in depth are generated by irradiation of Au and Ni nanowire arrays with femtosecond laser pulses of relativistic intensities. This volumetric plasma heating approach creates a new laboratory plasma regime in which extreme plasma parameters can be accessed with table-top lasers. The increased hydrodynamic-to-radiative lifetime ratio is responsible for a dramatic increase in the X-ray emission with respect to polished solid targets. The sequence of PIC maps in Fig. 1a shows that an intense femtosecond laser pulse can penetrate deeply into an array of vertically aligned Ni wires (diameter, 55 nm) where it is nearly totally absorbed (Fig. 1b). The simulation describes all the phases of nanowire heating, explosion and volume plasma formation. Local field enhancement[21], field fluctuations and resonance heating[14] are all described by the code. However, because the average density is much higher than the critical density and the nanowire spacing is much smaller than the laser wavelength, bulk resonances are not present. Optical field ionization (OFI) is active at the boundary of the nanowires where vacuum heating of electrons takes place[24]. The hot electron population drives collisional electron impact ionization deep into the nanowire core (OFI is insufficient to ionize beyond $Z = 18$), causing the plasma to rapidly reach an electron density of 2×10^{24} cm^{-3} (left frames in Fig. 1c). Despite the high average electron density, the laser pulse propagates deeply inside the nanostructured material as long as the gaps between the nanowires are free from plasma. Free electrons inside the nanorods are bound by collective fields and do not contribute to the plasma refractive index. The high energy deposited into the nanowire cores is transformed into a thermal energy density of ~2 GJ cm^{-3}, with average thermalized electron energy of 4 keV over the penetration depth and ~8 keV near the nanowire tips. The heated nanowire plasmas rapidly expand radially until the plasma fills the vacuum gaps. Beyond this point, any further propagation of laser light deep into the target is effectively terminated by the formation of a critical density surface. The ultrashort duration of the laser pulse allows for the majority of the energy to be efficiently deposited before gap closure. Hot plasma formation starts at the tip of the wire and propagates along the wires towards the supporting

[1]Department of Electrical Computer Engineering, Colorado State University, Fort Collins, Colorado 80523, USA, [2]Institut für Theoretische Physik, Heinrich-Heine-Universität Düsseldorf, 40225 Düsseldorf, Germany, [3]Department of Chemistry, Colorado State University, Fort Collins, Colorado 80523, USA, [4]Department of Physics, Colorado State University, Fort Collins, Colorado 80513, USA. *e-mail: jorge.rocca@colostate.edu

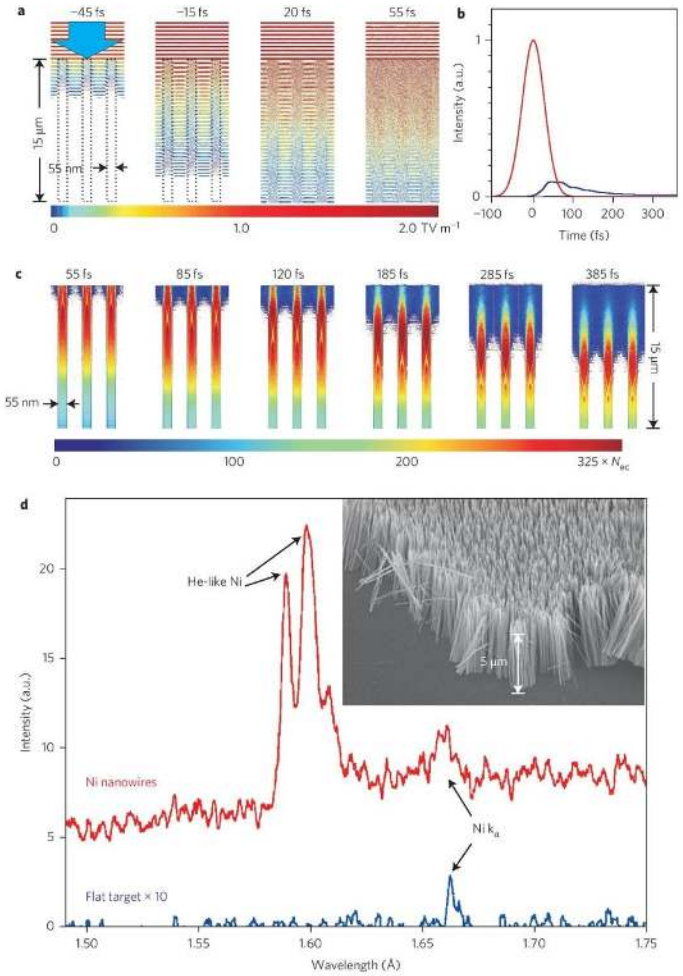

Figure 1 | PIC simulation and spectra from plasma generated by femtosecond pulse irradiation of a vertically aligned array of 55-nm-diameter Ni nanowires. a, PIC simulations of the penetration of the laser beam electric field in an array of 15-μm-long Ni wires with an average atomic density of 12% solid density irradiated at an intensity of 5×10^{18} W cm^{-2} by a $\lambda = 400$ nm, 60 fs (FWHM) duration laser pulse. Times are measured with respect to the peak of the laser pulse. The laser field scale is in units of TV m^{-1}. **b**, Computed impinging (red) and reflected (blue) laser intensity. **c**, Computed electron density evolution. The electron density scale is in units of critical density ($N_{ec} = 7 \times 10^{21}$ cm^{-3}). **d**, Single-shot X-ray spectra comparing the emission from an irradiated array of 5-μm-long, 55-nm-diameter Ni nanowires to that from a flat polished Ni target. The nanowire target plasma spectrum is dominated by He-like Ni resonance and intercombination line emission. The latter is merged with several $1s2p^2$-$1s^22p$ lines from Li-like Ni. The only line observed in the flat target plasma spectra is the Ni-k_α line. Inset: scanning electron microscope image of the array of vertically aligned nanowires.

substrate (Fig. 1c). Our simulations show that 385 fs after the peak of laser irradiation a fibre length of several micrometres has 'burned' (Fig. 1c), creating a plasma layer with an average density of 3×10^{23} cm^{-3} and an electron temperature of 2–4 keV, in which an extremely high degree of ionization is rapidly reached by collisional electron impact ionization.

We irradiated arrays of vertically aligned Ni and Au nanowires with ultrahigh-contrast ($>1 \times 10^{11}$) pulses of ~60 fs full-width at half-maximum (FWHM) duration from a frequency-doubled ($\lambda =$ 400 nm) high-power Ti:sapphire laser. The ultrahigh contrast is critical, as a relatively low-intensity pre-pulse can destroy the array by forming a critical density surface before the arrival of the

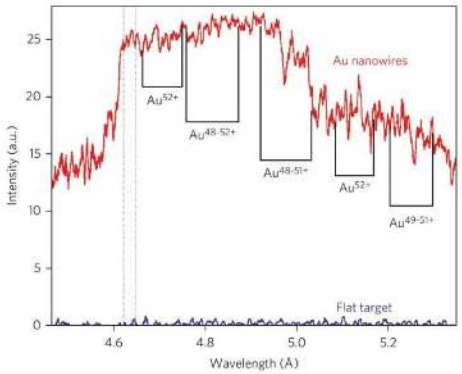

Figure 2 | Single-shot M-shell spectra of vertically aligned arrays of 80-nm-diameter Au nanowires compared with the spectra from a flat, polished Au target. The target is irradiated at an intensity of 5×10^{18} W cm^{-2} with a high-contrast $\lambda = 400$ nm wavelength laser pulse of 60 fs (FWHM) duration. Brackets highlight regions where the emission is dominated by Co-like, Ni-like, Cu-like, Zn-like and Ga-like Au ions. The dashed lines define the region where there is a contribution from the k_α line of Cu, which originates from a Cu layer at the base of the Au nanowires.

high-intensity ultrashort pulse. The laser beam was focused to reach an intensity of 5×10^{18} W cm^{-2} onto the target using an off-axis parabolic mirror. Arrays of 55- and 80-nm-diameter nanowires with an average density of ~12% solid density were synthesized by electrodeposition in anodic aluminium oxide membranes[25]. The X-ray emission was simultaneously monitored with a von Hamos crystal spectrometer oriented at a 45° angle from the target surface and with an array of four filtered Si photodiodes. Figure 1d shows a single-shot spectrum of the emission in the 1.5–1.75 Å region for a plasma created from vertically aligned Ni nanowires (55 nm diameter) separated by 135 nm. Strong emission is observed from the $2p$–$1s$ ($\lambda = 1.588$ Å) and intercombination lines of He-like Ni (Ni^{+26}), with the latter merged with Li-like Ni lines. This spectrum differs dramatically from that for a polished flat target irradiated under the same conditions, which only shows line emission from the Ni k_α line at 1.658 Å (with ×10 magnified scale in Fig. 1d). The k_α emission is produced mainly by high-energy electrons, while generation of the He-like ion transitions requires a hot thermal plasma to generate and excite the highly stripped ions. It is remarkable that the He-like line emission from the nanowire target exceeds the intensity of the k_α line at this irradiation intensity, because in previous work with Cu foils, the emission from the k_α lines was only surpassed at irradiation intensities $>2 \times 10^{20}$ W cm^{-2} (ref. 11). The aligned Ni nanowire target produced a greater than 50-fold increase in X-ray flux in this 7–8 keV spectral region. Similar enhancements were also observed in the 1 keV photon energy region, in agreement with previous experiments[20]. Similarly, a near solid density Au plasma with an extraordinarily high degree of ionization was created by irradiating an array of 80-nm-diameter Au wires (length, 5 μm). The Au nanowire spectrum in Fig. 2 (for $\lambda = 4.5$–5.25 Å) displays strong Au M-shell emission with unresolved 4-3 lines from ions ranging from Co-like (Au^{+52}) to Ga-like (Au^{+48}) Au (ref. 26). Both the spectra and the filtered photodiode array signals from the Au targets show a dramatic increase in X-ray yield compared with flat polished solid targets when irradiated by the same pulse. The spectra show increases by up to a factor of 100 in emission in the 2.3–2.75 keV photon regions. Filtered photodiode measurements show a 50-fold emission increase for photon energies >8 keV. Spectra obtained for arrays of 35- and 80-nm-diameter nanowires also display strong He-like line emission, in agreement with the prediction of the PIC simulation.

The depth to which the Ni nanowire target is ionized to the He-like state was determined experimentally to be 3–4 μm by

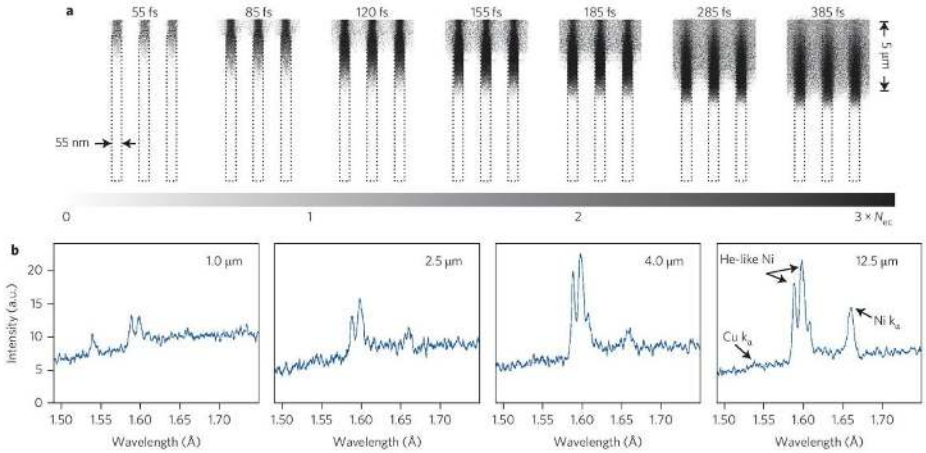

Figure 3 | Generation of He-like ions in the volumetrically heated Ni plasmas. a, PIC simulation maps showing the evolution of the density of He-like nickel ions. The He-like ion density is in units of critical electron density ($N_{ec} = 7 \times 10^{21}$ cm^{-3}). The wires have diameters of 55 nm, and the array has an average atom density of 0.12 solid. Irradiation intensity = 5×10^{18} W cm^{-2}. **b**, X-ray emission of nanowire targets of four different lengths: 1.0, 2.5, 4.0 and 12.5 μm. He α emission is observed to saturate for wire lengths greater than 4 μm, suggesting a plasma volume 3–4 μm deep is heated sufficiently for ionization to reach the He-like stage.

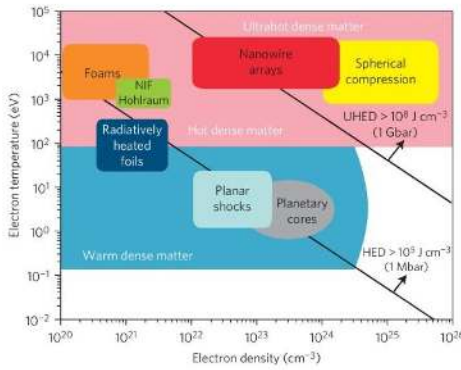

Figure 4 | Parameter space of temperature–electron density showing the plasma regime accessible by irradiation of aligned nanowire arrays relative to other high-energy density plasmas. The lines show the approximate limit of the region commonly accepted as high-energy density (HED, $>1 \times 10^5$ J cm^{-3}) and the region defined as ultrahigh-energy density (UHED, $>1 \times 10^8$ J cm^{-3}).

monitoring the spectrally resolved X-ray emission as a function of nanowire length. Figure 3b shows spectra from arrays of 55-nm-diameter Ni nanowires of four different lengths between 1 μm and 12.5 μm. The intensity of the He-like line is observed to increase with nanowire length until it saturates for a length of ~4 μm, beyond which it remains virtually unchanged. In contrast, the k_α emission continues to increase beyond this length as the fast electrons interact with a larger volume of neutral atoms. The PIC simulations reproduce the experimental results in showing that a plasma depth of several micrometres is volumetrically heated to reach the He-like ion stage. Figure 3a shows that 385 fs after the peak of the irradiation pulse a plasma depth of ~5 μm is computed to be ionized to the He-like stage. This large increase in heated plasma volume relative to plasmas from flat solid targets irradiated under the same conditions significantly lengthens the plasma hydrodynamic time. Simultaneously, the radiative lifetime is greatly decreased as a result of the nearly two orders of magnitude increase in plasma density, the higher temperature, and higher average Z of the nanowire plasma. The combination of these two effects results in a greatly decreased cooling time to hydrodynamic time ratio, a key parameter governing X-ray conversion efficiency. This and the increase in plasma density explain the dramatic increase in X-ray yield observed in nanowire plasma experiments.

Other plasma parameters are computed to be exceptional. The wire core is calculated to reach thermal pressures of 10 Gbar and a thermal energy density of 2 GJ cm^{-3}, while the plasma created after the dissolved wires expand, collide and thermalize is computed to have a thermal energy density of 0.3 GJ cm^{-3} and a pressure of 1–2 Gbar. This pressure is nearly two orders of magnitude larger than that in inertial confinement fusion Hohlraum plasmas[27] and is comparable to that created in the central hot spot of the imploded fusion capsule in the early National Ignition Facility (NIF) experiments at ultrahigh laser energy[4]. The nanowire plasma conditions are surpassed only by those obtained when the NIF capsule is highly compressed[3], effectively creating a new laboratory plasma regime (Fig. 4). Furthermore, our simulations predict that irradiation of vertically aligned nanophotonic arrays with highly relativistic intensities will reach unprecedented degrees of ionization in dense laboratory plasmas. For example, irradiation of a uranium nanowire array with laser intensities of 1×10^{20} W cm^{-3} can be expected to generate plasma densities of 1×10^{24} cm^{-3}, dominated by atoms ionized >70 times.

Methods

The nanowire arrays were irradiated with laser pulses ($\lambda = 400$ nm; ~60 fs duration; up to 0.5 J energy) generated by frequency-doubling the output of a Ti:sapphire ($\lambda = 800$ nm) laser delivering pulses of 2 J energy. The pulse duration was monitored on a shot-to-shot basis using single-shot frequency-resolved optical gating (FROG) operating at the fundamental wavelength. Contrast of the 1ω beam was measured using a third-order scanning autocorrelator and was found to be limited to $\sim 2 \times 10^{-7}$ by an amplified spontaneous emission (ASE) pedestal preceding the main pulse. This contrast was increased to $>1 \times 10^{11}$ by frequency-doubling in a 6-cm-diameter, 0.8-mm-thick, KDP Type I crystal. Four dichroic mirrors with coatings designed to reflect 99.9% of the 2ω beam and transmit 98.5% of the 1ω beam were used to separate the 2ω beam from the fundamental. The pulse energy was measured on every shot with a pyroelectric energy meter placed after a 500-μm-thick beamsplitter with a coating designed to reflect 1% of the pulse energy. The 2ω beam was focused onto the target at normal incidence using an $f = 17.8$ cm Al-coated off-axis parabolic mirror. The nanowire arrays were synthesized by electrodeposition in anodic aluminium oxide membranes[25]. After dissolving the alumina membrane, arrays of free-standing parallel nanowires with a high degree of order were exposed. All samples were imaged with a scanning electron microscope before the experiment.

The X-ray emission in the 1.5–1.75 Å and 4.5–5.5 Å ranges was measured using an efficient von Hamos crystal that was mounted at an angle of 45° with respect to the target normal. The spectrometer was operated in the third order of a cylindrically bent mica crystal (radius = 2 cm) with filters consisting of 183 μm Mylar + 50 μm Al for the Ni spectra, and 13 μm Mylar for the Au spectra. In addition, to stop visible light, the linear charge-coupled device was covered with a filter consisting of 1 μm Mg deposited on 3 μm Mylar. Line identification of the Ni spectra was performed using data from the NIST Atomic Spectra Database, and that of the Au spectra primarily using the work from Busquet *et al.*[26], complemented by data from May *et al.* and Scofield *et al.* (referenced in the Supplementary Information). The X-ray emission was simultaneously monitored using an array of filtered Si photodiodes.

The simulations were conducted with the fully electromagnetic PIC code VLPL (Virtual Laser-Plasma Laboratory)[28]. The full three-dimensional geometry was used. We assumed that Ni nanowires with a diameter of 55 nm were arranged in an array with a periodicity of 135 nm. The laser pulse was modelled by a plane wave with the time envelope $a(t) = a_0 \exp(-t^2/\tau^2)$, where the relativistic amplitude $a_0 = eA/mc^2 = 0.75$ corresponds to a laser intensity of $I_0 = 4.8 \times 10^{18}$ W cm^{-2} and a pulse duration $\tau = 40$ fs (60 fs FWHM) impinging at normal incidence on the nanowire array. The standard PIC algorithm was extended by packages for OFI, binary collisions and electron impact ionization. The OFI was treated as an under-barrier tunnelling in the static electric field[29,30]. Only sequential field ionization was considered. The binary collisional package calculated probabilities of Coulomb collisions between all particles in one mesh cell. The code was run on 256 processors of a local Intel-Nehalem cluster.

Received 27 March 2013; accepted 18 July 2013; published online 1 September 2013

References

1. Glenzer, S. H. *et al.* Symmetric inertial confinement fusion implosions at ultra-high laser energies. *Science* **327,** 1228–1231 (2010).
2. Fujiota, S. *et al.* X-ray astronomy in the laboratory with a miniature compact object by laser-driven implosion. *Nature Phys.* **5,** 821–825 (2009).
3. Robey, H. F. *et al.* Hohlraum-driven mid-Z (SiO_2) double-shell implosions on the Omega Laser Facility and their scaling to NIF. *Phys. Rev. Lett.* **103,** 145003 (2009).
4. Glenzer, S. H. *et al.* Cryogenic thermonuclear fuel implosions on the National Ignition Facility. *Phys. Plasmas* **19,** 1228–1231 (2012).
5. Fournier, K. B. *et al.* Efficient multi-keV X-ray sources from Ti-doped aerogel targets. *Phys. Rev. Lett.* **92,** 165005 (2004).
6. Matthews, D. L. *et al.* Characterization of laser produced plasma X-ray sources for use in X-ray radiography. *J. Appl. Phys.* **54,** 4260–4268 (1983).
7. Foord, M. E. *et al.* Ionization processes and charge-state distribution in a highly ionized high-Z laser-produced plasma. *Phys. Rev. Lett.* **85,** 992–995 (2000).
8. Heeter, R. F. *et al.* Benchmark measurements of the ionization balance of non-local- thermodynamic-equilibrium gold plasmas. *Phys. Rev. Lett.* **99,** 195001 (2007).
9. Young, B. K. F., Wilson, B. G., Price, D. F. & Stewart, R. E. Measurement of X-ray emission and thermal transport in near-solid-density plasmas heated by 130 fs laser pulses. *Phys. Rev. E* **58,** 4929–4936 (1998).
10. Guethlein, G., Foord, M. E. & Price, D. Electron temperature measurements of solid density plasmas produced by intense ultrashort laser pulses. *Phys. Rev. Lett.* **77,** 1055–1058 (1996).

11. Theobald, W. *et al.* Hot surface ionic line emission and cold K-inner shell emission from petawatt-laser-irradiated Cu foil targets. *Phys. Plasmas* **13,** 043102 (2006).
12. Hobbs, L. M. *et al.* Demonstration of short pulse laser heating of solid targets to temperatures of 600 eV at depths of 30 μm using the Orion high power laser. *Bull. Am. Phys. Soc.* **57,** 156 (2012).
13. Huntington, C. M. *et al.* Spectral analysis of X-ray emission created by intense laser irradiation of copper materials. *Rev. Sci. Instrum.* **83,** 10E114 (2012).
14. Ditmire, T. *et al.* High-energy ions produced in explosions of superheated atomic clusters. *Nature* **386,** 54–56 (1997).
15. Murnane, M. M. *et al.* Efficient coupling of high-intensity subpicosecond laser pulses into solids. *Appl. Phys. Lett.* **62,** 1068–1070 (1993).
16. Gordon, S. P., Donnelly, T., Sullivan, A., Mamster, H. & Falcone, R. W. X-rays from microstructured targets heated by femtosecond lasers. *Opt. Lett.* **19,** 484–487 (1994).
17. Rajeev, P. P. Taneja, P., Ayyub, P., Sandhu, A. S. & Kumar, G. Metal nanoplasmas as bright sources of hard X-ray pulses. *Phys. Rev. Lett.* **90,** 115002 (2003).
18. Sumeruk, H. A. *et al.* Control of strong-laser-field coupling to electrons in solid targets with wavelength-scale spheres. *Phys. Rev. Lett.* **98,** 045001 (2007).
19. Khattak, F. Y. *et al.* Enhanced He-α emission from 'smoked' Ti targets irradiated with 400 nm, 45 fs laser pulses. *Europhys. Lett.* **72,** 242–248 (2005).
20. Kulcsár, G. *et al.* Intense picosecond X-ray pulses from laser plasmas by use of nanostructured 'velvet' targets. *Phys. Rev. Lett.* **84,** 5149–5152 (2000).
21. Mondal, S. *et al.* Highly enhanced hard X-ray emission from oriented metal nanorod arrays excited by intense femtosecond laser pulses. *Phys. Rev. B* **83,** 035408 (2011).
22. Ovchinnikov, A. V. *et al.* Characteristic X-rays generation under the action of femtosecond laser pulses on nano-structured targets. *Laser Particle Beams* **29,** 249–254 (2011).
23. Nishikawa, T., Suzuki, S., Watanabe, Y., Zhou, O. & Nakano, H. Efficient water-window X-ray pulse generation from femtosecond-laser-produced plasma by using a carbon nanotube target. *Appl. Phys. B* **78,** 885–890 (2004).
24. Brunel, F. Not-so-resonant, resonant absorption. *Phys. Rev. Lett.* **59,** 52–55 (1987).
25. Prieto, A. L. *et al.* Electrodeposition of ordered Bi_2Te_3 nanowire arrays. *J. Am. Chem. Soc.* **123,** 7160–7161 (2001).
26. Busquet, M., Pain, D., Bauche, J. & Luc-Koenig, E. Study of X-ray spectrum of laser-produced Au plasmas. *Phys. Scripta* **31,** 137–148 (1985).
27. MacGowan, B. J. *et al.* Laser–plasma interactions in ignition scale Hohlraum plasmas. *Phys. Plasmas* **3,** 2029–2040 (1996).
28. Pukhov, A. Three-dimensional electromagnetic relativistic particle-in-cell code VLPL (Virtual Laser Plasma Lab). *J. Plasma Phys.* **61,** 425–433 (1999).
29. Zhidkov, A. & Sasaki, A. Effect of field ionization on interaction of an intense subpicosecond laser pulse with foils. *Phys. Plasmas* **7,** 1341–1344 (2000).
30. Karmakar, A. & Pukhov, A. Collimated attosecond GeV electron bunches from ionization of high-Z material by radially polarized ultra-relativistic laser pulses. *Laser Particle Beams* **25,** 371–377 (2007).

Acknowledgements

This work was supported by a Defense Threat Reduction Agency grant (HDTRA-1-10-1-0079) and by the HEDLP programme of the Office of Science of the US Department of Energy. The experiments were conducted at facilities from the National Science Foundation (NSF) ERC for Extreme Ultraviolet Science and Technology at Colorado State University using equipment develop under NSF grant MRI-ARRA 09-561. A.P. acknowledges support from DFG funded project TR18. The authors acknowledge the contributions of D. Ryan, C. Benton, A. Nobel and M. Woolston in relation to the experimental set-up, E. Jackson for nanowire target fabrication and C. Menoni and D. Patel for providing high-damage-threshold coatings. The authors thank J. Reader, J. Gillaspy, A. Kramida and J. Curry from NIST, Gaithersburg, for providing the atomic spectral data used to interpret the spectra, and R. London, R. Lee and M. Schneider for discussions and references.

Author contributions

V.N.S. and J.J.R. conceived the experiment. A.Pu. developed the PIC model and performed the simulations. J.J.R. and M.A.P. designed the experiment. M.A.P., R.H., C.B. and J.J.R. carried out the experiment and acquired the data. Y.W., B.M.L. and J.J.R. developed the ultrashort pulse laser. Y.W., L.Y. and S.W. contributed to making the laser operational for the experiments and R.H., A.P. and C.B. developed the nanowire targets. V.N.S. conducted hydrodynamic simulations and V.N.S., A.Pu. and J.J.R. interpreted the simulations. M.A.P., J.J.R., V.N.S. and A.Pu. wrote the paper, with contributions from the other authors.

Additional information

Supplementary information is available in the online version of the paper. Reprints and permissions information is available online at www.nature.com/reprints. Correspondence and requests for materials should be addressed to J.J.R.

Competing financial interests

The authors declare no competing financial interests.

Appendix II

Related work on laser-created plasmas published during the duration of the Ph.D program

1. J. Filevich, J. Grava, **M. Purvis,** M. C. Marconi, and J. J. Rocca, J. Nilsen, J. Dunn, and W.R. Johnson, "Prediction and observation of tin and silver plasmas with index of refraction greater than one in the soft x-ray range", Physical Review E 74, 016404, (2006).
2. J. Filevich, J. Grava, **M. Purvis**, M. C. Marconi, J. J. Rocca, J. Nilsen, J. Dunn, and W. R. Johnson, "Multiply ionized carbon plasmas with index of refraction greater than one", Laser and Particle Beams 25, 1 (2007).
3. **M. Purvis**, J. Grava, J. Filevich, M. C. Marconi, J. J. Rocca, J. Dunn, S. J. Moon, V. N. Shyaptsev, E. Jankowska, "Dynamics of converging laser-created plasmas in semi-cylindrical cavities studied using soft x-ray laser interferometry", Physical Review E, 76, 046402 (2007).
4. J. Grava, **M.A. Purvis,** J. Filevich, M.C. Marconi, J.J. Rocca, J. Dunn, S.J. Moon, V.N. Shlyaptsev, "Dynamics of a dense laboratory plasma jet investigated using soft x-ray laser interferometry," Physical Review E, 78, 016403 (2008).
5. J. Nilsen, J.I. Castor, C.A. Iglesias, K.T. Cheng, J. Dunn, W.R. Johnson, J. Filevich, **M.A. Purvis**, J. Grava, and J.J. Rocca, "Understanding the anomalous dispersion of doubly-ionized carbon plasmas near 47 nm," High Energy Density Physics, 4, pg 107-113, (2008).
6. **M. Purvis**, J. Grava, J. Filevich, M.C. Marconi, J. Dunn, S.J. Moon, V.N. Shlyaptsev, E. Jankowska, and J.J. Rocca, "Soft x-ray laser interferometry of colliding laser-created plasmas in semi-cylindrical cavities," IEEE Transactions on Plasma Sciences 36, 4, 1134, (2008).
7. J. Grava, **M.A. Purvis**, J. Filevich, M.C. Marconi, J. Dunn, S.J. Moon, V.N. Shlyaptsev, and J.J. Rocca, "Soft X-Ray Laser Interferometry of a Dense Plasma Jet", IEEE Transactions on Plasma Sciences 36, 4, 1286, (2008).
8. J. Nilsen, J. I. Castor, C.A. Iglesias, K.T. Cheng, J. Dunn, W.R. Johnson, J. Filevich, **M.A. Purvis**, J. Grava, J. J. Rocca,, "Understanding the anomalous dispersion of doubly ionized carbon plasmas near 47nm." High Energy Density Physics, 4 (2008).
9. J. Dunn, E. W. Magee, R. Shepherd, H. Chen, S. B. Hansen, S. J. Moon, G. V. Brown, M.-F. Gu, P. Beiersdorfer, and **M. A. Purvis**, "High resolution soft x-ray spectroscopy of low Z K-shell emission from laser-produced plasmas," Rev. Sci. Instrum. 79, 10E314 (2008), DOI:10.1063/1.2968704
10. J. Filevich, **M. Purvis**, J. Grava, D.P. Ryan, J. Dunn, S.J. Moon, V.N. Shlyaptsev, and J.J. Rocca, "Bow shocks formed by plasma collisions in laser irradiated semi-cylindrical cavities," High Energy Density Physics (2009), doi: 10.1016/j.hedp.2009.04.003
11. J. Colgan, J. Abdallah Jr., C. J. Fontes, D. P. Kilcrease, J. Dunn, **M. Purvis**, and R.W. Lee, "Non-LTE and gradient effects in K-shell oxygen emission laser-produced plasma," High Energy Density Physics (2010), doi:10.1016/j.hedp.2010.01.015

12. **M. A. Purvis**, J. Grava, J. Filevich, D. P. Ryan, S. J. Moon, J. Dunn, V. N. Shlyaptsev and J. J. Rocca, "Collimation of dense plasma jets created by low-energy laser pulses and studied with soft x-ray interferometry," Physical Review E 81, (2010).
13. N. Rohringer, D. Ryan, R.A. London, **M. Purvis,** F. Albert, J. Dunn, J. D. Bozek, C. Bostedt, A. Graf, R. Hill, S. P. Hau-Riege, and J. J. Rocca, Nature 481, 488.
14. K. C. Cone, H. A. Baldis, J. Dunn, M. J. May, **M.A. Purvis**, M.B. Schneider, and H.A. Scott, "Time-resolved soft x-ray spectra from laser-produced Cu plasma, Rev. Sci. Inst. 83, (2012).
15. C. Weninger, **M. Purvis**, D. Ryan, R. A. London, J. D. Bozek, C. Bostedt, A. Graf, G. Brown, J. J. Rocca, and N. Rohringer, Stimulated Electronic X-ray Raman Scattering, Phys. Rev. Lett. 111, (2013).
16. **M. A. Purvis**, V.N. Shlyaptsev, R. Hollinger, C. Bargsten, A. Pukhov, A. Prieto, Y. Wang, B. M. Luther, L. Yin, S. Wang, and J. J. Rocca. Relativistic plasma nano-photonics for ultra-high energy density physics, Nature Photonics 7, 796-780 (2013).